bioRxiv preprint doi: https://doi.org/10.1101/421586; this version posted September 19, 2018. The copyright holder for this preprint (which was not certified by peer review) is the author/funder. All rights reserved. No reuse allowed without permission.

Emergent oscillations in dense adaptive cell populations

Shou-Wen Wang[1,2,*] and Lei-Han Tang[1,3,4,†]

[1] *Beijing Computational Science Research Center, Beijing, 100094, China*
[2] *Department of Engineering Physics, Tsinghua University, Beijing, 100086, China*
[3] *Department of Physics and Institute of Computational and Theoretical Studies, Hong Kong Baptist University, Hong Kong, China*
[4] *State Key Laboratory of Environmental and Biological Analysis, Hong Kong Baptist University, Hong Kong, China*

(Dated: September 18, 2018)

Dynamical quorum sensing is one of the simplest group behaviours in cell populations, where collective oscillations emerge via mutual signaling beyond a critical cell density. Although many examples are documented, no unifying principle has yet been proposed. Here, by considering the response of cells to the extracellular signal and vice versa, we develop a quantitative theory for the phenomenon, and present a necessary condition for collective oscillations in a communicating population. We further show that a sufficient condition for oscillations is fulfilled by adaptive cells which reset their signal secretion rate upon prolonged stimulation. These general results were elucidated from non-equilibrium thermodynamic principles, where active cells play the role of engines to power oscillations in the medium. This unexpected link between adaptation and oscillation is shown to underlie several known examples of dynamical quorum sensing, and as such may also be a source of inadvertent group behaviour in large populations of living organisms.

The use of a pacemaker to direct temporal progression of developmental processes is widespread in biology. During mound formation of starved social amoebae, cyclic AMP waves guide migrating cells towards the high density region [1, 2, 15, 16]. Elongation of the vertebrate body axis proceeds with a segmentation clock [5, 14]. Multicellular pulsation has also been observed in nerve tissues [7], yeast cell suspensions [8, 24, 26], during dorsal closure in late stage drosophila embryogenesis [11], and more [12–14]. In these examples, communication through chemical or mechanical signals is essential to excite otherwise non-oscillatory cells. Dubbed "dynamical quorum sensing", this class of behaviour lies outside the well-known Kuramoto paradigm of oscillator synchronization [15].

Traditionally, rate-equation models of molecular reactions and their regulation are adopted to explain auto-induced oscillations in specific systems [16, 17]. Development of these models typically follow an iterative process built on the accumulation of experimental data. While this approach has been effective in dealing with well-characterized biochemical pathways, progress has been slow in resolving the dynamics of more complex intracellular networks due to the proliferation of unknown model parameters and interactions. Recent advances in high-resolution imaging and microfluidics offer new opportunities to quantify cell-to-cell communication in a range of environmental conditions [18, 21]. This prompted us to examine collective oscillations in terms of whole-cell response to external perturbations, with the aim to uncover higher level organizational principles.

Here, we report a generic condition for collective oscillations to emerge, and show that it is satisfied when cells are able to adapt to an external signal, i.e., they reset their response to prolonged external stimulation. In particular, we prove the existence of an "active" frequency regime, where an adaptive cell outputs energy upon external stimulation. We show that one frequency out of this active regime is selected and amplified spontaneously when a cell population, beyond a critical size, interacts through the shared signal. This leads to sustained collective oscillations. The nonequilibrium mechanism is shown to underlie several known examples of dynamical quorum sensing, and might even be implicated in the long-standing puzzle of glycolytic oscillations, which awaits testing. We discuss the implications of this general mechanism at the end of the paper.

Necessary conditions for collective oscillations

Fig.1**a** presents a generic description of a communicating cell population. The extracellular signal s is taken to be the concentration of molecules sensed and released by participating cells. The "sender activity" of a given cell is described by a variable a immediately upstream of signal release. Its dynamics is controlled by an intracellular regulatory network that responds to s through receptor proteins. To see how the sender activities might disrupt quiescence in an equilibrium state of s, we consider the following dynamical equation:

$$\gamma_s \dot{s} = -K_s s + \sum_{j=1}^{N} \alpha_2 a_j. \tag{1}$$

Here $-K_s s$ describes restoration of quiescence through signal degradation or dilution, and the sum represents disturbance created by activities of N cells in a unit volume, with a prefactor $\alpha_2 > 0$. The meaning of constants

* wangsw09@csrc.ac.cn; Current Address: Department of Systems Biology, Harvard Medical School, Boston, MA 02115, USA
† lhtang@csrc.ac.cn

bioRxiv preprint doi: https://doi.org/10.1101/421586; this version posted September 19, 2018. The copyright holder for this preprint (which was not certified by peer review) is the author/funder. All rights reserved. No reuse allowed without permission.

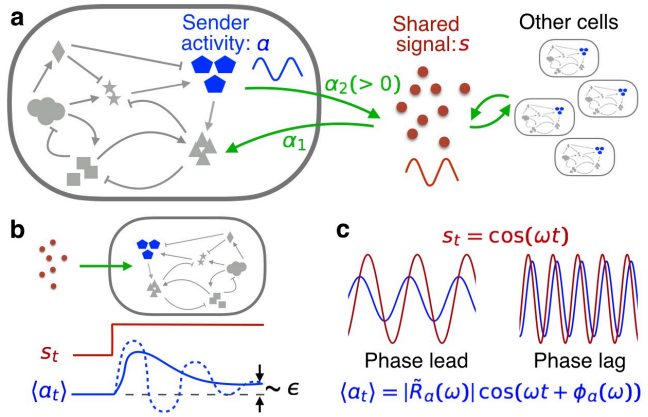

FIG. 1. **Spontaneous oscillations in a population of adaptive senders. a**, Cells communicate via a shared signal s. The sender activity a of a cell is regulated by a hidden intracellular network that responds to s. **b**, Adaptation of sender activity to a stepwise signal: after a transient response, a returns to its pre-stimulus state (within a small error ϵ). Two examples are shown (solid and dashed line). **c**, Response of a to an oscillatory signal. The phase shift ϕ_a switches sign, allowing energy outflow from an adaptive sender at selected frequencies.

γ_s, K_s and α_2 will become clear later. At the same time, under a small perturbation of the extracellular signal, the average response of an individual cell's activity satisfies

$$\langle a_t \rangle = \int_{-\infty}^{\infty} R_a(t-\tau) s_\tau d\tau, \tag{2}$$

with $\langle \cdot \rangle$ denoting the noise average and the stationary activity set to be zero. The response function R_a encodes the property of the complex intracellular signaling network.

The shared signal s offers a means to synchronize the sender activities. We derive here a matching condition for s and a's to enter a collectively oscillating state. In the Fourier space, Eq. (2) becomes $\langle \tilde{a}(\omega) \rangle = \tilde{R}_a(\omega)\tilde{s}(\omega)$. For simplicity, we assume a homogeneous population with the same response. Then, Eq. (1) gives $\tilde{s}(\omega) = N\alpha_2 \tilde{R}_s(\omega)\tilde{a}(\omega)$, where $\tilde{R}_s = (K_s - i\gamma_s\omega)^{-1}$, with i the imaginary unit. Combining these two equations, we obtain $\langle \tilde{a}(\omega) \rangle = N\alpha_2 \tilde{R}_a(\omega)\tilde{R}_s(\omega)\langle \tilde{a}(\omega) \rangle$. This equation applies to the quiescent or weakly oscillatory regime, but not the fully-developed oscillations (otherwise nonlinear effects have to be considered). At the *onset* of collective oscillations, $\langle \tilde{a}(\omega_o) \rangle \neq 0$, and we have $N_o\alpha_2 \tilde{R}_a(\omega_o)\tilde{R}_s(\omega_o) = 1$. To gain more insight, we decompose the response spectrum $\tilde{R}_a$ into the amplitude $|\tilde{R}_a|$ and the relative phase shift ϕ_a, i.e. $\tilde{R}_a \equiv |\tilde{R}_a| \exp(-i\phi_a)$, and also $\tilde{R}_s \equiv |\tilde{R}_s| \exp(-i\phi_s)$. Then, the cell density N_o and frequency ω_o at the onset of collective oscillations need to satisfy

$$\phi_a(\omega_o) = -\phi_s(\omega_o), \tag{3a}$$

$$|\tilde{R}_a(\omega_o)\tilde{R}_s(\omega_o)| = (\alpha_2 N_o)^{-1}. \tag{3b}$$

As the cell number further increases, the oscillations continue to develop and nonlinearity becomes important. The whole population might resume the quiescent state at a large cell density. We note that Eq. (1) warrants a lagged response (i.e., $-\pi < \phi_s < 0$). Hence, Eq. (3a) demands sender activities to lead the signal.

The phase-leading requirement can be well understood in the context of non-equilibrium energetics [1]. For this we imagine that Eq. (1) describes an overdamped particle in a passive medium, where γ_s is the friction coefficient, $-K_s s$ the restoring force, and $\sum_j \alpha_2 a_j$ the collective external force exerted on the particle. In this analogy, $\phi_s \in (-\pi, 0)$ actually corresponds to the dissipative nature of this particle. This can be proved generically for passive systems using the Fluctuation-Dissipation Theorem (FDT) [6] that demands the imaginary part of $\tilde{R}_s(\omega)$ to be positive. On the other hand, a leading phase enables energy outflow under periodic stimulation. We have calculated the work done by one of the cells when the signal oscillates at a frequency ω. The output power $\dot{W} \equiv \langle \dot{s} \cdot \alpha_2 a \rangle$ is found to be proportional to $\alpha_2\omega|\tilde{R}_a(\omega)| \sin\phi_a(\omega)$. This energy flux is positive when a has a phase lead over s, re-affirming Eq. (3a) on thermodynamic grounds. Additional details of this perspective can be found in Supplementary Part 2.

Adaptation route to collective oscillations

Previously, a phase-leading response to a low frequency signal has been reported in the activity of *E. coli* chemoreceptors [18] and in the displacement of hair bundles to mechanical stimulation [22]. In both cases, the system's response to a stepwise signal ramp is adaptive, i.e., the activity in question returns to its pre-stimulus level up to an "adaptation error" ϵ, as illustrated in Fig. 1**b**. Adaptation implies vanishing response to slow perturbations, i.e., $\lim_{\omega\to 0} \tilde{R}'_a(\omega) \sim \epsilon$. We show that this property is sufficient to achieve phase-leading response in a range of frequencies. For this we recall that, as a result of causality, the real ($\tilde{R}'_a$) and imaginary ($\tilde{R}''_a$) part of $\tilde{R}_a(\omega)$ satisfy the Kramers-Krönig relation [2]:

$$\tilde{R}'_a(\omega) = \frac{2}{\pi}\int_0^{\infty} \tilde{R}''_a(\omega_1)\frac{\omega_1}{\omega_1^2 - \omega^2} d\omega_1. \tag{4}$$

Combined with the requirement of adaptation, we obtain

$$\tilde{R}'_a(0) = \int_0^{\infty} \tilde{R}''_a(\omega_1)\omega_1^{-1} d\omega_1 \sim \epsilon. \tag{5}$$

Hence, for sufficiently accurate adaptation, $\tilde{R}''_a(\omega)$ must change sign across the frequency domain. In other words, both phase-leading ($\tilde{R}''_a < 0$) and lagged ($\tilde{R}''_a > 0$) behaviour are present across the frequency domain, as illustrated in Fig. 1**c**. The existence of a phase-leading response for adaptive systems, on general grounds, yields a sufficient condition for Eq. (3a) to be satisfied and thus for oscillations to occur beyond a critical cell density.

There are a variety of intracellular regulatory schemes by which adaptation can be achieved [9, 24]. As a con-

bioRxiv preprint doi: https://doi.org/10.1101/421586; this version posted September 19, 2018. The copyright holder for this preprint (which was not certified by peer review) is the author/funder. All rights reserved. No reuse allowed without permission.

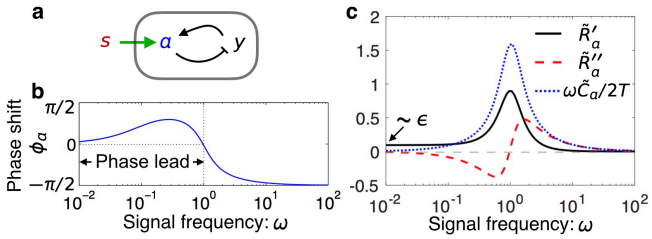

FIG. 2. **Spectral properties of an adaptive variable**. **a**, A noisy two-component model with negative feedback. **b**, Phase shift of a with respect to s from the response spectrum $\tilde{R}_a(\omega) = |\tilde{R}_a(\omega)| \exp(-i\phi_a(\omega))$. The phase shift ϕ_a switches from negative (phase-lag) to positive (phase-lead) as the frequency decreases. **c**, Real ($\tilde{R}'_a$) and imaginary ($\tilde{R}''_a$) components of the response spectrum. $\tilde{R}'_a$ is of order ϵ in the zero frequency limit, while $\tilde{R}''_a$ changes sign as frequency increases. Also shown is the correlation spectrum $\tilde{C}_a(\omega)$ multiplied by $\omega/(2T)$, where T is the noise strength. The fluctuation-dissipation theorem $\tilde{R}''_a = \omega\tilde{C}_a(\omega)/(2T)$ for thermal equilibrium systems is satisfied on the high frequency side, but violated at low frequencies, a signature of non-equilibrium effect. Parameters: $\tau_a = \tau_y = \alpha_1 = c_3 = 1$, $\epsilon = 0.1$.

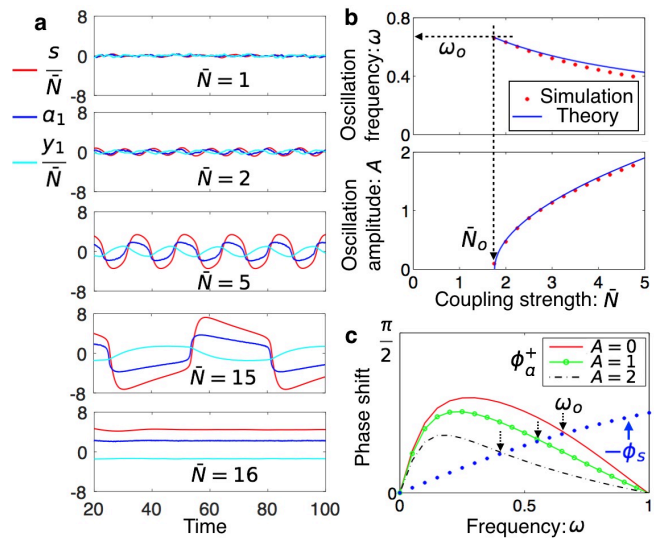

FIG. 3. **Collective oscillations of coupled adaptive circuits.** **a**, Time traces of the signal (red) and of sender activity (blue) and memory (cyan) from one of the participating cells at various values of the coupling strength $\bar{N} = \alpha_1\alpha_2 N$. **b**, The oscillation frequency ω and amplitude A against $\bar{N}$. Onset of oscillations is of the Hopf bifurcation type. **c**, Determination of oscillation frequency from a renormalized phase matching condition at finite oscillation amplitudes A. Parameters: $\tau_a = \tau_y = \gamma_s = K_s = c_3 = 1$, $\alpha_1 = \alpha_2 = 0.5$, and $\epsilon = 0.1$. The strength of noise terms is set at $T = 0.01$.

crete example, we considered a noisy two-component negative feedback model where the signal couples directly to the sender activity a with a strength $\alpha_1 > 0$ (Fig. 2**a** and Methods). In Fig. 2**b**, we show the numerically exact phase shift of a. As predicted, $\phi_a(\omega)$ undergoes a sign change. Correspondingly, the imaginary component of the response $\tilde{R}''_a$ becomes negative in the phase-leading regime, violating the FDT (Fig. 2**c**) as a result of the out-of-equilibrium dynamics [5, 8, 26, 27, 30].

We performed numerical experiments by adopting this circuit for each cell and coupling them via Eq. (1). Fig. 3**a** shows time traces of the signal s (red) together with sender activity a (blue) and memory variable y (cyan) from one of the cells. As the effective coupling constant $\bar{N} \equiv N\alpha_1\alpha_2$ increases, the coupled system goes from quiescence with weak background fluctuations to oscillating and then back to quiescence, as suggested before. In the oscillatory regime, the sender activity a leads s to enable energy outflow from the cell.

What is the nature of the transition to collective behavior for this system? Our numerical results suggest that the oscillation amplitude A of sender activity increases following a square-root law, implying a transition of the Hopf bifurcation type (Fig. 3**b**, red dots). To fully understand it, we extend the matching condition Eq. (3) to predict not only the onset of oscillations but also how it grows, by using the renormalized response spectra that incorporate the nonlinear effects associated with finite oscillation amplitudes. The analysis successfully predicts the onset coupling $\bar{N}_o \simeq 1.7$ and frequency $\omega_o \simeq 0.7$, and also yields the observed frequency shift and square-root law in quantitative agreement with simulation data (Fig. 3**b**, blue curves). As a visualization of this analysis, Fig. 3**c** shows the renormalized phase shift ϕ_a^+ at three selected oscillation amplitudes. The phase ϕ_s of the signal response function is independent of A due to the linearity of Eq. (1). Intercept of the two phase shift curves yields the oscillation frequency at a given A and furthermore a value for $\bar{N}$ from a renormalized form of Eq. (3b). A more complete discussion of this procedure is given in Supplementary Part 3.

Collective oscillations have also been observed previously in coupled excitable systems, where each cell is described by the FitzHugh-Nagumo model [12, 14, 15]. Can we understand this phenomenon in terms of adaptation? Actually, in the quiescent state, return of the system to its resting state upon a signal ramp can be considered as a special form of adaptation, although the excursion is much amplified (Supplementary Fig. 3). Therefore the general arguments we developed still apply. Sporadic firing triggered by noise blurs transition to the oscillating state. Nevertheless, when there is sufficient averaging over a large population size, our theory based on the averaged response of individual cells well predicts the threshold coupling strength $\bar{N}_o$ and frequency ω_o (Supplementary Fig. 5). Calculation of the frequency shift upon further increase of the cell density requires careful treatment of the intrinsic nonlinear effects at the group level which is beyond the scope of this study (Supplementary Fig. 5-6).

Experimental systems utilizing adaptation

In several known examples of emergent oscillations,

bioRxiv preprint doi: https://doi.org/10.1101/421586; this version posted September 19, 2018. The copyright holder for this preprint (which was not certified by peer review) is the author/funder. All rights reserved. No reuse allowed without permission.

we found strong evidence for adaptive sender activity. The first one is otoacoustic emission, where sound is generated in the inner ear by an array of oscillating hair cells [13, 14]. Here, acoustic wave in the extracellular fluid acts as a mechanical signal to couple hair cells. Each hair cell possesses hair bundles that respond adaptively to the stimulus with the help of molecular motors. Remarkable experiments have confirmed that hair bundles are active systems with an anticipatory response (i.e., phase-leading) [22]. The second one is extracellular cAMP waves during aggregation of starved social amoebae. An earlier experimental work attributed pulsation at the origin of the wave to cells' excitable response [15]. A more recent experiment [16] provided direct evidence of adaptation in the cytosolic cAMP concentration against fold change of the extracellular cAMP concentration. The third example is found in collective oscillations in synthetic quorum sensing populations [17] (See Supplementary Fig. 7 for details). Lastly, we mention the very recent work on segmentation clock in the presomitic mesoderm (PSM), where dynamical quorum sensing by the PSM cells is reported [14]. The authors invoked a phenomenological excitable dynamics to interpret oscillatory behaviour seen in their experiments. It would be interesting to associate dynamical variables in their model with the physical processes of mechanosensing and cytoskeleton remodeling, in analogy with other adaptive systems considered above.

Glycolytic oscillations: adaptation or synchronization?

Finally, we turn to the long-standing problem of glycolytic oscillations in yeast cell suspensions [8]. Pulsation in the intracellular nicotinamide adenine dinucleotide (NADH) concentration is triggered by shutting down the respiratory pathway. The freely diffusing molecule acetaldehyde (ACE) mediates cell-to-cell communication. Despite decades of intense exploration, interpretation of various experimental findings remains controversial [21, 24, 26]. Here, we focus on a model of yeast glycolysis proposed in [19], whose predictions on phase relationships of metabolites agree well with experiments (Supplementary Fig. 11). The model contains around 20 metabolic reactions (Fig. 4**a**). Using extracellular glucose and ACE concentrations as control parameters, we computed the response of all metabolites along the glycolytic pathway to an ACE signal. Different types of behaviour were found as illustrated in Figs. 4**b**-**d**. The white region in Fig. 4**b** marks spontaneous oscillations reported previously [21]. It is bordered by the newly identified regions (blue and orange) where a subset of metabolites, notably ATP, exhibit adaptive behaviour. However, the concentration of pyruvate (PYR), the substrate for the reaction to produce ACE, is adaptive and phase-leading over the signal only in the blue region (Fig. 4**d**).

Closer examination of the response curves to a sinusoidal signal revealed phase-synchronization of

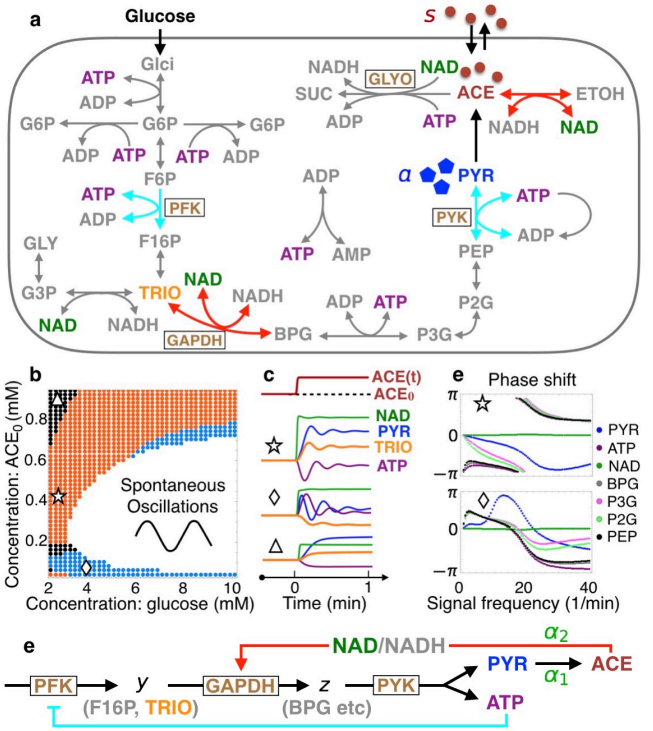

FIG. 4. **Yeast glycolytic oscillations**. **a**, The reaction network of glycolysis in an yeast cell. **b**, Single-cell response diagram spanned by the extracellular glucose and acetaldehyde (ACE) concentrations that control respectively the glycolytic flux and redox state inside the cell. Each colored region corresponds to a particular type of response of metabolite concentrations to a stepwise ramp of the extracellular ACE concentration (**c**). **d**, Frequency-resolved phase shifts of selected metabolites to weak sinusoidal perturbations. Adaptation occurs in both the orange and blue region, while phase lead of PYR over ACE is restricted to the blue region. **e**, A reduced model for glycolytic oscillations where the intracellular NAD/NADH ratio and pyruvate (PYR) act as the receiver and sender of the signal (ACE), respectively. Adaptive response of PYR to ACE is coupled to the homeostasis of ATP through the reaction PYK.

metabolites connected by fast reactions. Focusing on the response of the network on the low frequency side, we constructed a reduced model of four intracellular variables connected by three reactions as shown in Fig. 4**e**, taking into account stoichiometry and known regulatory interactions [24]. Increase of GAPDH reaction rate by an upshift of ACE concentration (part of the front redox loop) is offset by the negative feedback loop to maintain ATP homeostasis. Consequently, the concentration of PYR, the "sender" of the redox signal, also adapts. The reduced model exhibits very similar response to ACE signal as in the full model (Supplementary Fig. 13), demonstrating insensitivity of the feedback mechanism to model details. On the other hand, we also found that elimination of the glyoxylate shunt (GLYO) flux in the reduced model enlarges the adaptive region (Supplementary Fig. 14). Consequently,

bioRxiv preprint doi: https://doi.org/10.1101/421586; this version posted September 19, 2018. The copyright holder for this preprint (which was not certified by peer review) is the author/funder. All rights reserved. No reuse allowed without permission.

coupled cells are able to oscillate collectively outside the white region in Fig. 4**a**, where the Kuramoto mechanism does not apply (Supplementary Fig. 16-18). It would be very interesting to establish the adaptive behaviour in microfluidic setups, where both the extracellular concentrations of ACE and glucose can be controlled precisely [21].

Discussion

Collective oscillations are ubiquitous in the biological world. Yet a good fraction of them, such as glycolytic oscillations, were observed only in lab conditions with no obvious functional relevance. In this work, we established a direct link between the group behaviour and another ubiquitous trait of living organisms, i.e., adaptive response to environmental perturbations. The biophysical principle yields renewed insights on the evolutionary origin of this collective phenomenon: on the one hand, collective behavior can be introduced through only minor innovations to molecular pathways; on the other hand, optimization of adaptive response to environmental variation may lead to undesired collective oscillations in a dense population. The latter can be considered as a tradeoff relation that shape the environmental response in living organisms.

An alternative scenario of collective oscillations would be through synchronization of oscillators, which is the well-known Kuramoto scenario [15]. Here, oscillations at the single-cell level emerge simultaneously with the group behavior. Hence, our work provides a complementary paradigm for collective oscillations. Two special cases of this principle have been reported before [16, 34], where nonlinear equations were adopted in their formulation. However, we found that linear response analysis is sufficient to describe the onset of collective oscillations. Furthermore, our arguments are robust against heterogeneities in the population as long as there are sufficient number of adaptive individuals whose active frequency regimes overlap with each other.

A great advantage afforded by the linear response formalism is its ability to organize knowledge about a single cell to predict whether and even when a given population enters a collective state, as in our case study of glycolytic oscillations. The response functions in question can be measured in single-cell experiments and model simulations. On the other hand, synthetic biology has become an important tool to produce spatiotemporal patterns [17, 35, 36]. It would be interesting to engineer cells with desired synthetic adaptive response to create novel collective behavior not long from now.

Methods

An adaptive model with negative feedback. The data presented in Figs. 2 and 3 were obtained from numerical integration of the coupled equations: $\tau_a \dot{a} = -a - c_3 a^3 + y + \alpha_1 s + \eta_a$, and $\tau_y \dot{y} = -a - \epsilon y + \eta_y$ [5, 26]. Here y is a memory node that implements negative feedback control on a, ϵ sets the adaptation error, and τ_a and τ_y are the intrinsic timescales for the dynamics of a and y, respectively. η_a and η_y are gaussian white noise with zero mean and correlators: $\langle \eta_a(t)\eta_a(\tau)\rangle = 2T\tau_a\delta(t-\tau)$ and $\langle \eta_y(t)\eta_y(\tau)\rangle = 2T\tau_y\delta(t-\tau)$, where $\delta(t)$ is the Dirac delta function. The cubic nonlinearity ($c_3 a^3$) is needed to limit cellular activity to a finite strength. For simplicity, we choose $\alpha_1 = 1$ so that the response function defined by $\tilde{R}_a(\omega) = \langle \tilde{a}(\omega)\rangle / \tilde{s}(\omega)$ can be compared with its equilibrium counterpart that satisfies the FDT $\tilde{R}''_a = \omega \tilde{C}_a(\omega)/(2T)$, with $\tilde{R}''_a$ denoting the imaginary component of $\tilde{R}_a$.

[1] P. Schaap, *Development* **138**, 387 (2011).
[2] T. Gregor, K. Fujimoto, N. Masaki, S. Sawai, *Science* **328**, 1021 (2010).
[3] A. E. Sgro, *et al.*, *Mol. Syst. Biol.* **11**, 779 (2015).
[4] K. Kamino, *et al.*, *Proc. Natl. Acad. Sci. U.S.A.* p. 201702181 (2017).
[5] A. Hubaud, O. Pourquié, *Nat. Rev. Mol. Cell Biol.* **15**, 709 (2014).
[6] A. Hubaud, I. Regev, L. Mahadevan, O. Pourquie, *Cell* **171**, 668 (2017).
[7] G. Buzsaki, *Rhythms of the Brain* (Oxford University Press, 2006).
[8] A. Goldbeter, *Biochemical oscillations and cellular rhythms* (Cambridge university press, 1997).
[9] S. De Monte, F. d'Ovidio, S. Danø, P. G. Sørensen, *Proc. Natl. Acad. Sci. U.S.A.* **104**, 18377 (2007).
[10] F. A. Chandra, G. Buzi, J. C. Doyle, *Science* **333**, 187 (2011).
[11] J. Solon, A. Kaya-Çopur, J. Colombelli, D. Brunner, *Cell* **137**, 1331 (2009).
[12] C. H. Ko, *et al.*, *PLoS Biol.* **8**, e1000513 (2010).
[13] D. T. Kemp, *J. Acoust. Soc. Am.* **64**, 1386 (1978).
[14] T. Reichenbach, A. Hudspeth, *Rep. Prog. Phys.* **77**, 076601 (2014).
[15] Y. Kuramoto, *Chemical oscillations, waves, and turbulence*, vol. 19 (Springer Science & Business Media, 2012).
[16] P. Mehta, T. Gregor, *Curr. Opin. Genet. Dev.* **20**, 574 (2010).
[17] A. Goldbeter, *Chaos* **27**, 104612 (2017).
[18] T. S. Shimizu, Y. Tu, H. C. Berg, *Mol. Syst. Biol.* **6**, 382 (2010).
[19] A.-K. Gustavsson, C. B. Adiels, B. Mehlig, M. Goksör, *Sci. Rep.* **5** (2015).
[20] K. Sekimoto, *Stochastic energetics*, vol. 799 (Berlin Springer Verlag, 2010).
[21] R. Kubo, *Rep. Prog. Phys.* **29**, 255 (1966).
[22] P. Martin, A. Hudspeth, F. Jülicher, *Proc. Natl. Acad. Sci. U.S.A.* **98**, 14380 (2001).
[23] J. Sethna, *Statistical mechanics: entropy, order parameters, and complexity*, vol. 14 (Oxford University Press, 2006).
[24] T.-M. Yi, Y. Huang, M. I. Simon, J. Doyle, *Proc. Natl.*

bioRxiv preprint doi: https://doi.org/10.1101/421586; this version posted September 19, 2018. The copyright holder for this preprint (which was not certified by peer review) is the author/funder. All rights reserved. No reuse allowed without permission.

Acad. Sci. U.S.A. **97**, 4649 (2000).
[25] W. Ma, A. Trusina, H. El-Samad, W. A. Lim, C. Tang, *Cell* **138**, 760 (2009).
[26] G. Lan, P. Sartori, S. Neumann, V. Sourjik, Y. Tu, *Nat. Phys.* **8**, 422 (2012).
[27] P. Sartori, Y. Tu, *Phys. Rev. Lett.* **115**, 118102 (2015).
[28] S.-W. Wang, Y. Lan, L.-H. Tang, *J. Stat. Mech.* **2015**, P07025 (2015).
[29] S.-W. Wang, K. Kawaguchi, S.-i. Sasa, L.-H. Tang, *Phys. Rev. Lett.* **117**, 070601 (2016).
[30] S.-W. Wang, *Phys. Rev. E* **97**, 052125 (2018).
[31] E. M. Izhikevich, *Dynamical systems in neuroscience* (MIT press, 2007).
[32] T. Danino, O. Mondragón-Palomino, L. Tsimring, J. Hasty, *Nature* **463**, 326 (2010).
[33] F. B. du Preez, D. D. van Niekerk, B. Kooi, J. M. Rohwer, J. L. Snoep, *FEBS J.* **279**, 2810 (2012).
[34] B. Lindner, J. Garcıa-Ojalvo, A. Neiman, L. Schimansky-Geier, *Physics Reports* **392**, 321 (2004).
[35] C. Liu, *et al.*, *Science* **334**, 238 (2011).
[36] L. Potvin-Trottier, N. D. Lord, G. Vinnicombe, J. Paulsson, *Nature* **538**, 514 (2016).

Acknowledges

The authors thank Caroline Adiels, Hugues Chaté, Terry Hwa, Kyogo Kawaguchi, Ben Machta, Yuhai Tu, Ned Wingreen, and Allon Klein for helpful discussions. The work is supported in part by the NSFC under Grant Nos. U1430237, 11635002 and U1530401, and by the Research Grants Council of the Hong Kong Special Administrative Region (HKSAR) under Grant No. 12301514.

Additional Information

See Supplementary.

bioRxiv preprint doi: https://doi.org/10.1101/421586; this version posted September 19, 2018. The copyright holder for this preprint (which was not certified by peer review) is the author/funder. All rights reserved. No reuse allowed without permission.

Supplementary for

Emergent oscillations in dense adaptive cell populations

Shou-Wen Wang*, Lei-Han Tang*
*Corresponding authors; Email: wangsw09@csrc.ac.cn, lhtang@csrc.ac.cn

CONTENTS

References 5

I. Introduction 7

II. Nonequilibrium thermodynamics of adaptive response 8
A. Phase-leading response of an adaptive variable 8
B. Energy outflow from an adaptive channel 8
C. The Fluctuation-Dissipation Theorem 9

III. A self-consistency scheme for frequency selection and oscillation amplitude determination 9
A. The phase matching condition and threshold cell density 10
B. The amplitude equations and frequency shift 10

IV. Adaptation route to collective oscillations in selected systems 13
A. The coupled excitable FitzHugh-Nagumo model 13
B. Collective oscillations in a synthetic circuit 16
C. Glycolytic oscillations in yeast cells 17
1. Single-cell perturbation study 19
2. A minimal model for glycolytic oscillations 21

References 26

I. INTRODUCTION

This supplementary contains derivations of various theoretical results stated in the Main Text, as well as exploration of a number of model systems. In view of the recent experimental studies on dynamical quorum sensing, we shall mainly focus on auto-induced collective oscillations of cells mediated by a chemical signal. However, to the extent that the underlying microscopic processes afford a thermodynamic description, our approach also applies in other physical contexts, e.g. mechanical or electrical signaling. We are particularly interested in exploring the nonequilibrium aspects of "activity" dynamics in a living cell. Concepts and tools from the recently developed stochastic thermodynamics [1] are used to map out the pattern of energy flow, complementing the descriptive modeling based on rate equations.

The material is organized as follows. Section II contains various mathematical results announced in the Main Text regarding the nonequilibrium response of an adaptive circuit and the associated energy flow. In Section III, we present a self-consistency scheme to predict the onset of auto-induced collective oscillations and its subsequent growth. The response functions that appear in the discussion can in principle be measured directly in experiments. In Section IV, we re-analyze collective oscillations in three representative model systems: the coupled FitzHugh-Nagumo (FHN) model with excitable units, a synthetic quorum sensing circuit, and glycolytic oscillations in yeast cell suspensions. An adaptive unit is identified in each of these systems, confirming the ubiquity of the proposed mechanism for collective oscillations. Furthermore, using the yeast glycolytic oscillations as an example, we demonstrate a computational procedure to reduce a complex and highly nonlinear network of biochemical reactions and regulation into a low dimensional one that still reproduces the main dynamical features of the original system.

bioRxiv preprint doi: https://doi.org/10.1101/421586; this version posted September 19, 2018. The copyright holder for this preprint (which was not certified by peer review) is the author/funder. All rights reserved. No reuse allowed without permission.

II. NONEQUILIBRIUM THERMODYNAMICS OF ADAPTIVE RESPONSE

A. Phase-leading response of an adaptive variable

Consider the temporal variation a_t of an intracellular observable a induced by a sinusoidal signal s_t from the environment at frequency ω. The amplitude of s_t is assumed to be small, so that it can be treated as a perturbation. The observable a is either directly or indirectly coupled to the signal s. On the scale of a single cell, both a_t and s_t may contain stochastic components. In the following, we shall examine the noise averaged response of a to the deterministic part of s, i.e., the signal. As usual, we use $\langle\cdot\rangle$ to denote the noise average. The following convention on forward and inverse Fourier transforms is adopted,

$$\tilde{f}(\omega) = \int_{-\infty}^{\infty} f(t)\exp(i\omega t)dt, \quad f(t) = \int_{-\infty}^{\infty} \tilde{f}(\omega)\exp(-i\omega t)\frac{d\omega}{2\pi}. \tag{S1}$$

In a steady-state, the ratio of the Fourier amplitudes $\langle\tilde{a}(\omega)\rangle$ and $\langle\tilde{s}(\omega)\rangle$ defines the response function $\tilde{R}_a(\omega) \equiv \langle\tilde{a}(\omega)\rangle/\langle\tilde{s}(\omega)\rangle$, which can be separated into its real $\tilde{R}'_a$ and imaginary $\tilde{R}''_a$ parts. (For a cellular variable a that follows stochastic dynamics, the ensemble averaged response is considered.) The well-known Kramers-Krönig relation from causality requirement on the response function states [2]:

$$\tilde{R}'_a(\omega) = \frac{2}{\pi}\int_0^{\infty} \tilde{R}''_a(\omega_1)\frac{\omega_1}{\omega_1^2-\omega^2}d\omega_1. \tag{S2}$$

In the case of a perfectly adapting a, the response vanishes under a sufficiently slow stimulus, i.e., $\lim_{\omega\to 0}\tilde{R}_a(\omega) = 0$. Equation (S2) then requires,

$$\int_0^{\infty} \tilde{R}''_a(\omega_1)\omega_1^{-1}d\omega_1 = 0. \tag{S3}$$

Consequently, $\tilde{R}''_a(\omega)$ must change sign at least once along the frequency axis. Let $\phi_a = -\arg(\tilde{R}_a)$ be the phase of $-\tilde{R}_a(\omega)$, with the minus sign introduced by convention. Positive and negative values of $\tilde{R}''_a$ thus translate to phase-lag ($-\pi < \phi_a < 0$) and phase-lead ($0 < \phi_a < \pi$) of a_t over s_t, respectively. By virtue of continuity, the sign change of $\tilde{R}''_a(\omega)$ is also expected in the partially adaptive case, provided the adaptation error $\epsilon \simeq \tilde{R}'_a(0)$ is sufficiently small.

B. Energy outflow from an adaptive channel

Auto-induced collective oscillations in a dissipative medium require an energy source. Below, we show that an active cell is able to output energy to a fluctuating s in the presence of an adaptive channel. The power of the output depends on the strength of the coupling as well as the amplitude and frequency of the fluctuating signal.

Consider a slightly more general form of Eq. (1) in the Main Text where the contribution from cell j to the total thermodynamic force on s is given by $O(a_j)$, which in general is nonlinear in a_j. The work done on s by the cell in a time interval $(0, L)$ can then be written as

$$W_j = \int_0^L O_t\dot{s}_t dt, \tag{S4}$$

where $O_t \equiv O(a_j(t))$ and s_t are both fluctuating quantities in general. We now consider a sinusoidal signal $s_t = s_0 + \Delta s\cos(\omega t)$ with a small amplitude Δs. To the first order in Δs, we have

$$O_t \simeq O_t^{(0)} + \Delta s|\tilde{R}_O(\omega)|\cos\big(\omega t + \phi_O(\omega)\big). \tag{S5}$$

Here $O_t^{(0)}$ denotes the stochastic trajectory of O in the absence of the sinusoidal signal. As usual, the linear response function R_O in the steady-state (ss) to a weak time-varying signal s_t is introduced through

$$\langle O_t\rangle \simeq \langle O\rangle_{ss} + \int_{-\infty}^{t} R_O(t-\tau)s_\tau d\tau, \tag{S6}$$

bioRxiv preprint doi: https://doi.org/10.1101/421586; this version posted September 19, 2018. The copyright holder for this preprint (which was not certified by peer review) is the author/funder. All rights reserved. No reuse allowed without permission.

where $\langle\cdot\rangle$ denotes average over noise. The phase angle $\phi_O(\omega) \equiv -\arg \tilde{R}_O(\omega)$. Substituting expression (S5) into Eq. (S4) and taking the limit $L \to \infty$, we obtain the time-averaged output power from the cell through this channel (omitting the subscript j),

$$\overline{\dot{W}} = \overline{O_t \dot{s}_t} + o\big((\Delta s)^2\big) = \frac{1}{2}\omega|\tilde{R}_O(\omega)| \sin\phi_O(\omega)(\Delta s)^2 + o\big((\Delta s)^2\big). \tag{S7}$$

Here the overline bar indicates averaging over time, and $o\big((\Delta s)^2\big)$ denotes terms higher than second order in Δs.

Given the relation $O_t = O(a_t)$, adaptation of the cellular variable a to a slow-varying s also implies the adaption of O to the signal. The causality condition (S2) applied to O_t then requires $\tilde{R}''_O(\omega) \equiv -|\tilde{R}_O(\omega)| \sin\phi_O(\omega) < 0$ in a certain frequency range. Consequently, Eq. (S7) predicts energy outflow from the channel under a periodic stimulation at these frequencies.

The discussion leading to Eq. (S7) in the previous section can be easily extended to the energy outflow under an arbitrary signal variation s_t with a power spectrum $\tilde{C}_s(\omega)$,

$$\overline{\dot{W}} = -\int d\omega\omega \tilde{R}''_O(\omega)\tilde{C}_s(\omega) + o(\Delta s^2), \tag{S8}$$

where Δs sets the overall amplitude of signal variation. If the cell were in thermal equilibrium, a would respond passively to a time-varying signal with a phase-lag and dissipate the energy inflow generated by the stimulation. An adaptive cell, on the other hand, is able to output energy in the form of work when stimulated in the right frequency range. This form of energy outflow is different from the heat dissipation arising from keeping the system out of equilibrium as studied in Refs. [3–5].

C. The Fluctuation-Dissipation Theorem

The fluctuation-dissipation theorem (FDT) is generally presented as an identity between the response function of a chosen variable to an external perturbation and the correlation function of the variable in question with the one that is conjugate to the perturbation[6]. For Markov systems which are of interest here, FDT holds when the detailed balance condition on the state-space transition rates is fulfilled. We refer the reader to Refs. [7, 8] for a detailed discussion, including more rigorous definitions of various quantities of interest.

Assuming that the signal s affects the cell through coupling to a conjugate variable O which is proportional to the variable a of interest, i.e., $O = c_0 a$ with c_0 a proportionality constant. In this case, FDT states that

$$\tilde{R}''_O(\omega) = \frac{\omega \tilde{C}_O(\omega)}{2T} > 0. \tag{S9}$$

Here, $\tilde{C}_O(\omega) = c_0^2\langle|\tilde{a}(\omega)|^2\rangle$ is the power spectrum of O_t which is always positive. Equation (S9) contradicts (S3), re-affirming that receptor adaptation cannot be realized without the presence of active processes inside the cell.

In Ref. [9], adaptation through a 3-node incoherent feed-forward motif was considered. It was later shown that the topology even supports adaptation in an equilibrium setting [10]. The main difference between these models and the receptor dynamics Eq. (3) in the Main Text is that, in the former, s not only couples to a directly, but also to other intracellular variables. The conjugate variable O is then a combination of a and other intracellular variables. We leave a detailed investigation of this issue to future work.

III. A SELF-CONSISTENCY SCHEME FOR FREQUENCY SELECTION AND OSCILLATION AMPLITUDE DETERMINATION

The thermodynamic analysis in the preceding section suggests the possibility of a positive feedback loop formed by a periodic signal and adaptive cells under generic conditions. Collective oscillations emerge when signal amplification by active cells overtakes signal dissipation in the passive medium. In this section, we examine this process in further detail and derive equations that can be used to determine the frequency and amplitude of auto-induced oscillations when the instability takes place. For simplicity, we shall consider a situation where diffusion of the signaling molecules in the medium is very fast so that spatial variations of s is suppressed. Consequently, the notion of a well-defined transition to the oscillating state can be introduced.

bioRxiv preprint doi: https://doi.org/10.1101/421586; this version posted September 19, 2018. The copyright holder for this preprint (which was not certified by peer review) is the author/funder. All rights reserved. No reuse allowed without permission.

A. The phase matching condition and threshold cell density

Given that individual cells couple to each other only through the signal field s, a self-consistency procedure similar to the solution of mean-field models in statistical physics can be employed. In this case, the linear equations governing an eigenmode with eigenvalue λ can be divided into subgroups associated with individual cells. The internal variables of a given cell appear in one and only one of the subgroups. Solution of the subset of equations for cell j yields the cell activity $\langle \tilde{a}_j \rangle = \tilde{R}_{a,j}(i\lambda)\langle \tilde{s} \rangle$. The function $\tilde{R}_{a,j}(i\lambda)$ is the same function introduced in the preceding section to describe the linear response of a_j to a sinusoidal perturbation at frequency $\omega = i\lambda$. Likewise, a response function $\tilde{R}_s(\omega)$ from the linearized relaxational dynamics of s can be obtained, treating contributions from cells as source terms, as in Eq. (1) of the Main Text. Combining the two steps, we arrive at the following eigenvalue equation for λ,

$$\tilde{R}_s(i\lambda) \sum_{j=1}^{N} \alpha_2 \tilde{R}_{a,j}(i\lambda) = 1. \tag{S1}$$

When a particular eigenvalue crosses the imaginary axis, its real part vanishes, while its imaginary part ω_o (the onset frequency) satisfies,

$$\alpha_2 N_o \tilde{R}_s(\omega_o) \tilde{R}_{\bar{a}}(\omega_o) = 1. \tag{S2}$$

Here $\tilde{R}_{\bar{a}}(\omega) \equiv N^{-1} \sum_{j=1}^{N} \tilde{R}_{a,j}(\omega)$ is the averaged single-cell response function.

Equation (S2) can be written separately for the phase shift $\phi = -\arg \tilde{R}$ and amplitude $|\tilde{R}|$ of the response functions. For $\alpha_2 > 0$, we have,

$$\phi_{\bar{a}}(\omega_o) = -\phi_s(\omega_o), \tag{S3a}$$

$$N_o = \frac{1}{|\alpha_2 \tilde{R}_s(\omega_o)||\tilde{R}_{\bar{a}}(\omega_o)|}. \tag{S3b}$$

Eq. (S3a) determines the frequency ω_o at the onset of collective oscillations, while Eq. (S3b) gives the threshold cell density N_o. As we mentioned in the Main Text, when the signal is passive, phase lead by the cell is required for Eq. (S3a) to be fulfilled. The explicit relation presented here complements the energy argument based on Eq. (S7), with the activity-generated thermodynamic force O_t being proportional to $\alpha_2 a_j$.

As it stands, the cell density N does not appear explicitly in the phase-matching condition (S3a). Therefore the frequency of collective oscillations can be estimated from separate measurements of the single-cell response and the medium response. In reality, it is conceivable that properties of the medium are affected by the presence of cells, e.g., the concentration of the signaling molecules secreted. Consequently, both $\tilde{R}_s(\omega)$ and $\tilde{R}_{\bar{a}}(\omega)$ may have certain weak dependence on N.

B. The amplitude equations and frequency shift

Beyond the initial instability, nonlinear effects need to be treated explicitly to determine the amplitude and frequency of oscillations. Assuming a periodic state, the signal strength $s(t)$ can be expressed as a Fourier series that includes the first harmonic as well as higher order harmonics produced by nonlinearities in the system dynamics. Likewise, the noise-averaged cellular activity $\langle a_j(t) \rangle$ can also be expressed as a Fourier series in t with the same basic frequency. For weak noise, the trajectory of the system falls on a well-defined limit cycle whose mean radius r sets the overall amplitude of oscillations, while the amplitude of the nth order harmonic scales as r^n. This structure allows for a systematic determination of the amplitudes using perturbation theory. Below, we illustrate the procedure in the case of cubic nonlinearities in both the dynamics for s and the dynamics for a, and comment on similarities and differences in more general situations. When the cell's activity is noisy, more sophisticated schemes based on the probability distribution function of the cellular state need to be introduced (see, e.g. Ref. [11]).

Let us consider a noiseless version of the adaptive dynamics defined by Eqs. (3) in the Main Text, together with a modified version of Eq. (1) that includes a cubic nonlinearity,

$$\tau_a \dot{a}_j = -(a_j - y_j) - c_3 a_j^3 + \alpha_1 s \tag{S4a}$$

$$\tau_y \dot{y}_j = -(a_j + \epsilon y_j) \tag{S4b}$$

$$\tau_s \dot{s} = -s - d_3 s^3 + \alpha_2 \sum_{j=1}^{N} a_j. \tag{S4c}$$

bioRxiv preprint doi: https://doi.org/10.1101/421586; this version posted September 19, 2018. The copyright holder for this preprint (which was not certified by peer review) is the author/funder. All rights reserved. No reuse allowed without permission.

Here $\tau_s = \gamma_s/K_s$ gives the relaxation timescale for the signal. We also set $\alpha_2 \to K_s\alpha_2$ for notational simplicity. The two coefficients c_3 and d_3 set the strengths of nonlinearities in the cellular and signal dynamics, respectively. The model has the inversion symmetry $s \to -s$ and $(a_j, y_j) \to (-a_j, -y_j)$, all j. Furthermore, if we redefine the sign of s and at the same time change the sign of α_1 and α_2, the equations remain the same.

We now seek a periodic solution to Eqs. (S4) in Fourier form,

$$s(t) = B\cos(\omega t) + \sum_{n=2}^{\infty} B^{(n)} \cos(n\omega t + \phi_s^{(n)}), \tag{S5a}$$

$$a_j(t) = A_j \cos(\omega t + \phi_{a,j}) + \sum_{n=2}^{\infty} A_j^{(n)} \cos(n\omega t + \phi_{a,j}^{(n)}), \qquad j = 1, \ldots, N, \tag{S5b}$$

$$y_j(t) = C_j \cos(\omega t + \phi_{y,j}) + \sum_{n=2}^{\infty} C_j^{(n)} \cos(n\omega t + \phi_{y,j}^{(n)}), \qquad j = 1, \ldots, N. \tag{S5c}$$

The amplitudes and phase shifts, all assumed to be real, satisfy a set of equations which can be derived by substituting Eqs. (S5) into Eqs. (S4), and grouping terms according to the order of the harmonic.

Starting from the first harmonic in the expressions (S5), the cubic terms in Eqs. (S4a) and (S4c) generate the first and third order harmonics according to the identity $(\cos\phi)^3 = (3\cos\phi + \cos 3\phi)/4$. Hence terms such as A_j^3 and B^3 are present in the equations for the first harmonic. On the other hand, the cubic nonlinearities do not generate even order harmonics if they are not included in the series initially. Hence, up to the third order in the amplitudes, the equations for the coefficients of the first harmonic take the form,

$$-i\omega\tau_a \tilde{a}_j \simeq -(1 + \frac{3}{4}c_3|\tilde{a}_j|^2)\tilde{a}_j + \tilde{y}_j + \alpha_1\tilde{s}, \tag{S6a}$$

$$-i\omega\tau_y \tilde{y}_j = -\tilde{a}_j - \epsilon\tilde{y}_j, \tag{S6b}$$

$$-i\omega\tau_s \tilde{s} \simeq -(1 + \frac{3}{4}d_3|\tilde{s}|^2)\tilde{s} + \alpha_2 \sum_j \tilde{a}_j. \tag{S6c}$$

Here we have introduced the short-hand notations $\tilde{s} = B, \tilde{a}_j = A_j \exp(-i\phi_{a,j})$, and $\tilde{y}_j = C_j \exp(-i\phi_{y,j})$.

To gain an intuitive understanding of the oscillatory solution as the cell density increases beyond the threshold N_o, we first eliminate the intracellular variable $\tilde{y}_j$ in Eqs. (S6a) and (S6b) to obtain,

$$\tilde{a}_j = \tilde{R}_{a,j}^{+}(\omega)\tilde{s}, \tag{S7}$$

where

$$\tilde{R}_{a,j}^{+}(\omega) \equiv \frac{\tilde{a}_j(\omega)}{\tilde{s}(\omega)} \simeq \frac{\alpha_1}{1 + 3c_3|\tilde{a}_j|^2/4 - i\omega\tau_a - 1/(i\omega\tau_y - \epsilon)} \tag{S8}$$

is a "nonlinear response function" which expresses the ratio of the complex amplitudes of the first harmonic on the limit cycle. Similarly, Eq. (S6c) can be rewritten as

$$\tilde{s} = \tilde{R}_s^{+}(\omega) \sum_{j=1}^{N} \alpha_2 \tilde{a}_j, \tag{S9}$$

where

$$\tilde{R}_s^{+}(\omega) \simeq \frac{1}{1 + 3d_3|\tilde{s}|^2/4 - i\omega\tau_s} \tag{S10}$$

is a "nonlinear response function" of s on the limit cycle. It is easy to see that $\tilde{R}_a^{+}(\omega)$ and $\tilde{R}_s^{+}(\omega)$ reduce to their respective linear counterparts $\tilde{R}_{a,j}(\omega)$ and $\tilde{R}_s(\omega)$ when the oscillation amplitudes vanish.

We now combine Eqs. (S7) and (S9) to obtain the self-consistency condition,

$$\alpha_2 N \tilde{R}_s^{+}(\omega)\tilde{R}_{\bar{a}}^{+}(\omega) = 1, \tag{S11}$$

which is reminiscent of Eq. (S2). Here $\tilde{R}_{\bar{a}}^{+}(\omega) \equiv N^{-1}\sum_{j=1}^{N} \tilde{R}_{a,j}^{+}(\omega)$ is the averaged single-cell nonlinear response function. When all cells are identical, $\tilde{R}_{\bar{a}}^{+}(\omega) = \tilde{R}_a^{+}(\omega)$. As before, Eq. (S11) can be rewritten in terms of the phase

bioRxiv preprint doi: https://doi.org/10.1101/421586; this version posted September 19, 2018. The copyright holder for this preprint (which was not certified by peer review) is the author/funder. All rights reserved. No reuse allowed without permission.

and amplitude of the nonlinear response functions,

$$\phi_{\tilde{a}}^{+}(\omega) = -\phi_{s}^{+}(\omega), \tag{S12a}$$

$$\alpha_2 N = \frac{1}{|\tilde{R}_s^{+}(\omega)||\tilde{R}_{\tilde{a}}^{+}(\omega)|}. \tag{S12b}$$

Formally, Eq. (S12a) can be used to determine the frequency shift at a finite amplitude of oscillation, while Eq. (S12b) relates the oscillation amplitude to the cell density N. Since the amplitudes enter quadratically into the nonlinear response functions, they are expected to increase as $(N - N_o)^{1/2}$ just above the threshold cell density N_o, e.g., the transition is of the Hopf bifurcation type.

In the Main Text, we have considered the case $c_3 = 1$ and $d_3 = 0$. Numerically, the oscillation frequency is found to decrease as the coupling strength $\bar{N} \equiv \alpha_1\alpha_2 N$ increases (see also Fig. S1**A**). This is consistent with Eq. (S12a) whose solution at selected oscillation amplitudes is shown in Fig. 3**C** in the Main Text. As the amplitude of the oscillations increase, $\phi_a^{+}(\omega)$ decreases on the low frequency side. Consequently, the intersection point with $\phi_s^{+}(\omega) = \phi_s(\omega)$ shifts to lower frequencies.

Interestingly, the limit cycle associated with the collective oscillation state in this model shrinks to a fixed point when $\bar{N}$ exceeds an upper threshold value $\bar{N}_b$. The dependence of $\bar{N}_b$ on the adaptation error ϵ, which is assumed to be small, can be estimated as follows. At a fixed point of Eqs. (S4) at $d_3 = 0$, we have $s \simeq \alpha_2 N a$ (from $\dot{s} = 0$), $y \simeq \alpha_1 s$ (from $\dot{a} = 0$), and $a \simeq \epsilon y$ (from $\dot{y} = 0$). Consequently, the upper threshold for oscillations has the scaling

$$\bar{N}_b \sim \frac{1}{\epsilon}. \tag{S13}$$

Figure S1**B** shows the numerical values for $\bar{N}_o$ and $\bar{N}_b$ against the adaptation error ϵ obtained in our simulations, which confirms (S13). The oscillating state expands over a larger range of cell densities when individual cells are more adaptive.

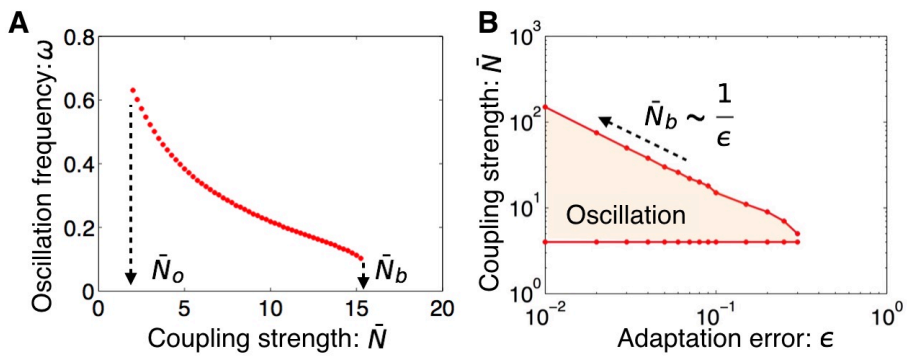

FIG. S1. **Collective oscillations in the model Eq. (S4) with nonlinear adaptation ($c_3 = 1$) and linear signal relaxation ($d_3 = 0$).** (**A**) Oscillation frequency against the effective cell density $\bar{N} = \alpha_1\alpha_2 N$. (**B**) The phase diagram in the plane spanned by $\bar{N}$ and the adaptation error ϵ. Other parameters are the same as in Fig. 3 of the Main Text.

Next, consider the case of nonlinear signal relaxation ($d_3 = 1$) and linear adaptation ($c_3 = 0$). The onset of collective oscillations is similar to the previous case (Fig. S2**A**), except that oscillations speed up as the cell density increases further. From Eq. (S10), we obtain

$$\phi_s^{+}(\omega) = -\arg \tilde{R}_s^{+}(\omega) = -\arctan\left[\frac{\omega}{\omega_s(1 + 3d_3|\tilde{s}|^2/4)}\right], \tag{S14}$$

which decreases as the oscillation amplitude increases. As shown in Fig. S2**B**, the intersection point shifts to the right. The predicted signal oscillation amplitude $B = |\tilde{s}|$ and frequency shift agree quantitatively with our numerical results (Fig. S2**C**).

In the more general case when both c_3 and d_3 are nonzero, we need to first express $\tilde{s}$ and $\tilde{a}_j$ in terms of a common variable that specifies oscillation amplitude before applying the phase-matching condition Eq. (S12a). As we see from the discussions above, depending on which of the two cubic nonlinearities is stronger, the oscillation frequency may shift either to lower or higher values. In general, nonlinearities may also be present in the dynamics of other intracellular variables which need to be dealt with case by case.

When quadratic nonlinearities are present in the system dynamics, the second harmonic is generated and need to be considered in the perturbative analysis. Consider for example the equation for a_j with an extra term $c_2 a_j^2$. Following

bioRxiv preprint doi: https://doi.org/10.1101/421586; this version posted September 19, 2018. The copyright holder for this preprint (which was not certified by peer review) is the author/funder. All rights reserved. No reuse allowed without permission.

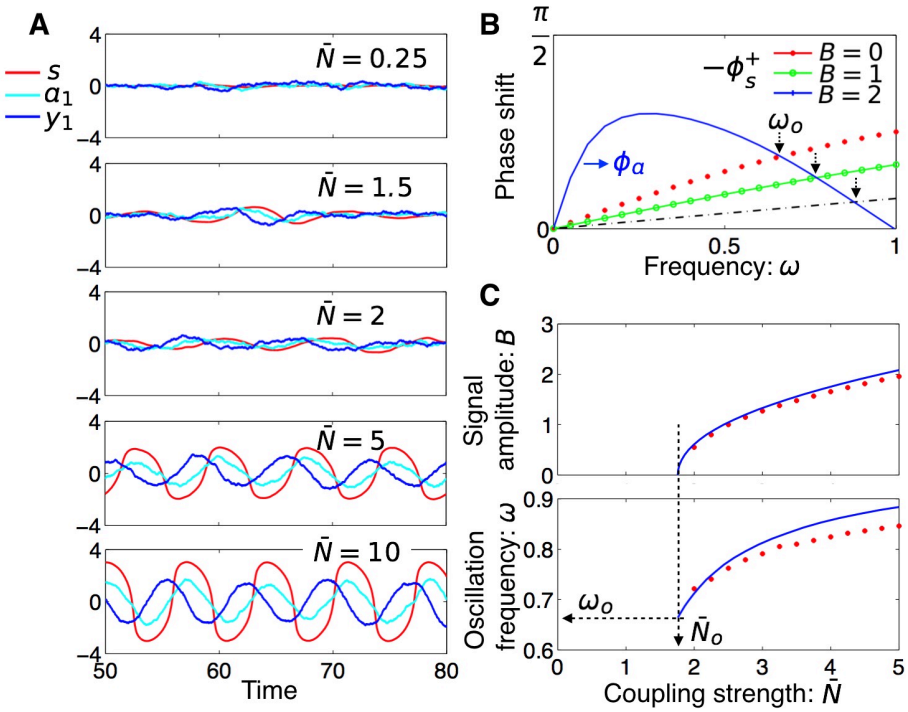

FIG. S2. **Collective oscillations in the model Eq. (S4) with linear adaptation ($c_3 = 0$) and nonlinear signal relaxation ($d_3 = 1$).** (**A**) Temporal trajectories at various values of $\bar{N}$. (**B**) The phase lead ϕ_a and lag $-\phi_s^+$ against ω at selected oscillation amplitudes. (**C**) The predicted oscillation frequency and amplitude as compared with those obtained from numerical simulations. Other parameters are the same as in Fig. 3 of the Main Text.

the same procedure that led to Eqs. (S6), we find an additional term $c_2\tilde{a}_j^*\tilde{a}_j^{(2)}$ on the right-hand side of Eq. (S6a), where $\tilde{a}_j^{(2)}$ is the amplitude of the second harmonic in $a_j(t)$ (including phase). The amplitude equation for the second harmonic relates $\tilde{a}_j^{(2)}$ to $c_2\tilde{a}_j^2$ and $\alpha_1\tilde{s}^{(2)}$. Together with the equation for $\tilde{s}^{(2)}$, amplitudes of the second harmonic can be expressed as a linear combination of terms $c_2\tilde{a}_j^2$ from different cells. The upshot of this exercise is that coefficient of the cubic term $|\tilde{a}_j|^2\tilde{a}_j$ in Eq. (S6a) should contain additional contributions proportional to c_2^2. The nonlinear response functions (S8) and (S10) on the limit cycle can still be defined in the same way, and Eq. (S11) still holds formally. Through $\tilde{s}^{(2)}$, terms $|\tilde{a}_k|^2$ from other cells enter the expression for $\tilde{R}_{a,j}^+(\omega)$. Two conclusions can be drawn from this fact: i) as in the case of cubic nonlinearities, the transition is still of the Hopf bifurcation type; ii) $\tilde{R}_{a,j}^+(\omega)$ can no longer be determined by simply measuring the response of a given cell to a sinusoidal stimulus at finite strength, as it is affected by the oscillation pattern of other cells in the system due to the quadratic nonlinearity.

IV. ADAPTATION ROUTE TO COLLECTIVE OSCILLATIONS IN SELECTED SYSTEMS

A. The coupled excitable FitzHugh-Nagumo model

We present here results on a coupled excitable FitzHugh-Nagumo (FHN) model often employed in the study of oscillatory phenomena in cell cultures [12] and developmental processes[13, 14]. A single FHN circuit takes the form,

$$\tau_a\dot{a}_j = a_j - a_j^3/3 - y_j + \alpha_1 s + \eta_{a_j}, \tag{S1a}$$

$$\tau_y\dot{y}_j = a_j - \epsilon y_j + a_0 + \eta_{y_j}. \tag{S1b}$$

The positive sign of the first term in the equation for a_j gives rise to excitability and a richer set of dynamical behavior than the simple adaptation of Eq. (S6), including the appearance of limit cycles and bistability when the parameters are tuned. The terms $\eta_{a_j}(t)$ and $\eta_{y_j}(t)$ represent gaussian white noise with $\langle\eta_{a_i}(t)\eta_{a_j}(t')\rangle = \langle\eta_{y_i}(t)\eta_{y_j}(t')\rangle = 2T\delta(t-t')\delta_{ij}$. Below, we limit ourselves to the parameter regime where individual circuits are excitable but not oscillating. In the absence of the stimulus s, each cell assumes the "resting state" with a mean activity $\langle a_j(t)\rangle = a_{rs}$.

bioRxiv preprint doi: https://doi.org/10.1101/421586; this version posted September 19, 2018. The copyright holder for this preprint (which was not certified by peer review) is the author/funder. All rights reserved. No reuse allowed without permission.

For small values of ϵ, the resting state activity $a_{rs} \simeq -a_0$ is nearly constant under a slow-varying $s(t)$. A sudden change of s or a sufficiently strong noise fluctuation, on the other hand, can send the circuit through a large excursion in the phase space (known as a "firing event") when the dynamics of y is slow (i.e., $\tau_y \gg \tau_a$). Figure S1**A** shows the noise-averaged response of the FHN circuit to a step signal of unit strength at $\epsilon = 0.1$. After a strong transient response, the value of $\langle a_j(t) \rangle$ returns to its pre-stimulus level within an interval of size ϵ. Therefore, despite the spontaneous firing of individual cells due to fluctuations, the noise-averaged response of an excitable cell is similar to the non-excitable case discussed in the preceding section. We have also calculated numerically the linear response function $\tilde{R}_a(\omega)$. The response amplitude $|\tilde{R}_a|$ peaks at an intermediate frequency, while phase-leading behavior is seen on the low frequency side (Fig. S1**B** and **C**).

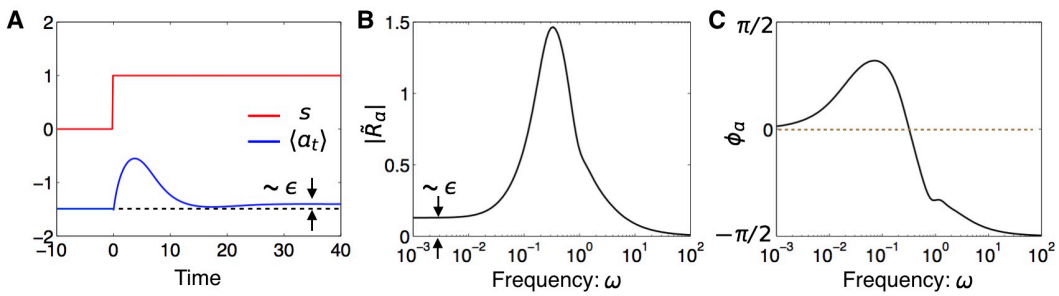

FIG. S1. **Noise-averaged response of the FHN circuit in the resting state**. (**A**) The average response to a step signal. (**B**) and (**C**) The response amplitude and phase shift of the circuit at various signal frequencies. Parameters: $\epsilon = 0.1$, $T = 0.1$, $\tau_a = 1$, $\tau_y = 5$, $a_0 = 1.5$, $\alpha_1 = 1$.

We now consider a system of N FHN circuits coupled together through a signal field whose dynamics is described by,

$$\tau_s \dot{s} = -s - s^3 + \alpha_2 \sum_j^N (a_j - a_{rs}). \tag{S1c}$$

As before we assume linear coupling between the signal and cellular activities which is expected to be a good approximation close to the onset of collective oscillations. A cubic term is introduced in Eq. (S1c) to suppress appearance of a limit cycle solution in the coupled system that pre-empts the continuous transition. Note that, without the cubic term, the substitution $s \to s/\alpha_1$ yields an effective coupling constant $\bar{N} = \alpha_1 \alpha_2 N$ when cells have identical noise-averaged behavior. This is no longer the case when the cubic term is present.

Fig. S2 shows our simulation results at selected values of $\bar{N}$. Here $a_1(t)$ and $a_2(t)$ are the activities of two out of a total of $N = 1000$ cells. The values of other parameters are given in the caption. At $\bar{N} = 0.1$, individual FHN circuits fire from time to time due to excitation by noise. However, the firing events are not synchronized and the signal level remains constant due to averaging. At $\bar{N} = 0.9$, collective behavior as seen in the oscillations of s starts to emerge, although individual circuits continue to fire sporadically. Upon further increase of $\bar{N}$, synchronized firing becomes more evident.

We now take a look at the oscillation amplitude and frequency near the onset of collective behavior. To compare with the theory presented in Sec. III, we computed the nonlinear response spectrum $\tilde{R}_a^+(\omega)$ of a single cell by simulating Eqs. (S1a) and (S1b) under a sinusoidal signal of finite amplitude B. The phase of the nonlinear response function at selected oscillation amplitudes is shown in Fig. S3**A**. For the parameters chosen, the onset frequency of oscillations is determined to be $\omega_o \approx 0.27$. Figs. S3**B** and **C** give the predicted amplitude and frequency from Eqs. (S12) against $\tilde{N}$ together with results from direct simulation of coupled FHN circuits. It is seen that very good agreement is reached for the onset coupling strength $\bar{N}_O$ and frequency ω_O, and for the dependence of the oscillation amplitude of s on $\tilde{N}$. However, opposite trend is seen in the predicted and actual frequency shift as the cell density or coupling strength increases.

Fig. S4 shows the power spectrum of $s(t)$ from simulations of the coupled system at two selected values of $\bar{N}$, one just above the onset of oscillations and the other in the developed region. In the latter case, the amplitude of the second harmonic becomes significant, invalidating the self-consistency approach developed in Sec. III that considers only the nonlinear response function of the circuit under a sinusoidal stimulus of finite amplitude. Furthermore, the FHN circuit (S1) does not have the inversion symmetry that prevents generation of even harmonics from odd ones. It is nevertheless interesting to see that the prediction of the oscillation amplitude near the onset still holds. In principle, a more elaborate self-consistency scheme involving nonlinear response to periodic stimuli containing higher

bioRxiv preprint doi: https://doi.org/10.1101/421586; this version posted September 19, 2018. The copyright holder for this preprint (which was not certified by peer review) is the author/funder. All rights reserved. No reuse allowed without permission.

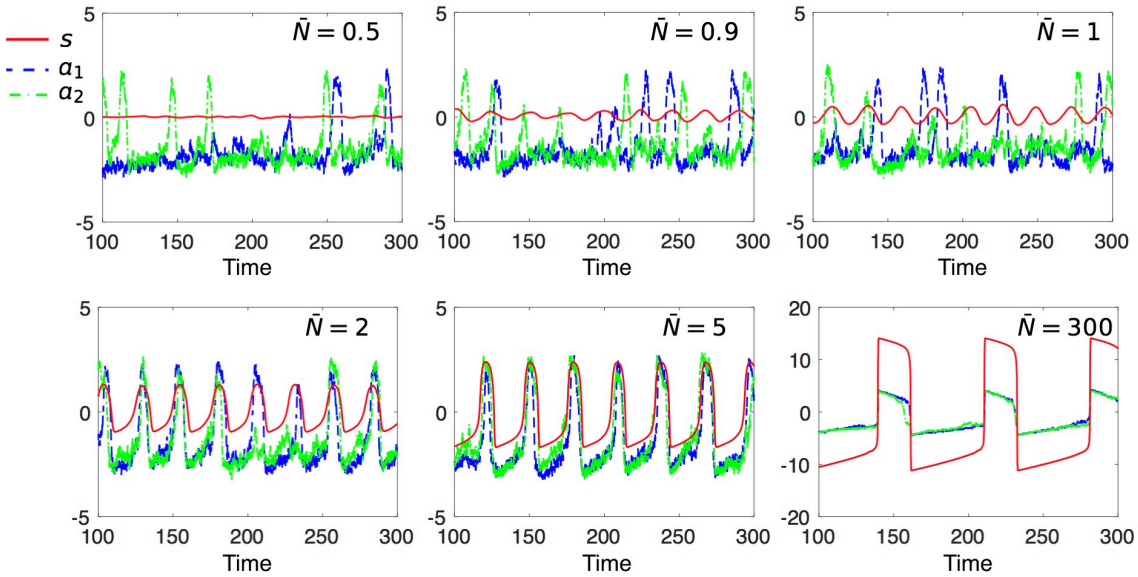

FIG. S2. **Trajectories of the coupled FHN model at various values of the effective coupling strength** $\bar{N}$. Except for the signal s, the activities of two out of a total of 1000 cells are plotted. Parameters: $\alpha_1 = 1$, $N = 1000$, $\epsilon = 0.1$, $T = 0.1$, $\tau_a = 1$, $\tau_y = 5$, $a_0 = 1.5$, and $\tau_s = 1$.

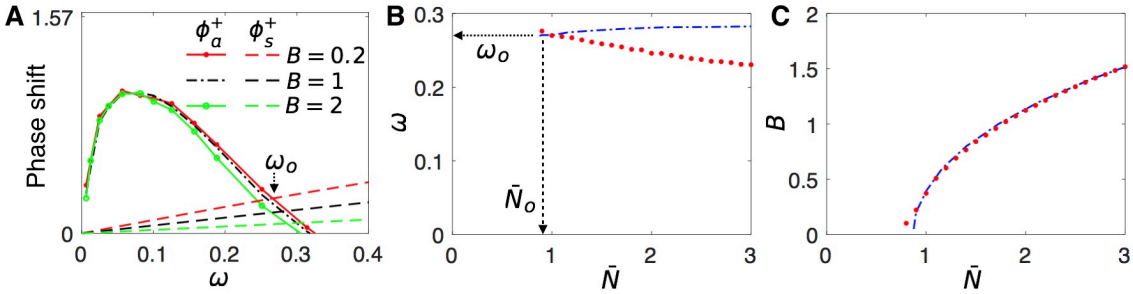

FIG. S3. **Oscillation frequency and amplitude of the coupled FHN model**. (**A**) Phase shifts of the nonlinear circuit (computed from numerical perturbation) and the signal (from analytical approximation) response against signal strength B. The intersection of ϕ_a^+ and ϕ_s^+ at a given B yields the predicted oscillation frequency. (**B**) and (**C**) Frequencies and amplitudes (blue dashed lines) predicted by the nonlinear response theory *vs* the actual ones (red stars, obtained from direct numerical simulation of the coupled model. Parameters are the same as in Fig. S2.

order harmonics can be developed, but in practice this will be much less useful due to the amount of data that need to be collected.

The model studied here shares many features with the one introduced earlier by Sgro *et al.* to describe dynamical quorum sensing in aggregates of social amoebae *Dictyostelium discoideum* [15], although the latter contains additional nonlinear effects. One such nonlinearity comes from the fact that a dicty cell detects extracellular cyclic AMP (cAMP) level s through a chemical binding mechanism. Therefore its activity responds to the signal through a change of the chemical potential of cAMP which is logarithmic in s, i.e., the linear term in s in Eq. (S1a) is replaced by $\log s$, dubbed "logarithmic sensing". Adaptation of cellular activity to the signal translates to a phenomenon known as "fold-change detection" which has been verified experimentally[16]. Another nonlinear effect comes from the massive release of cAMP to the extracellular environment in each firing event. As the cell density increases, the frequency of such events increases, and so is the cAMP level in the surrounding medium. When the adaptation is less than perfect, the increase in ambient cAMP concentration may also send individual cells into a recurrent firing state that synchronizes through the Kuramoto mechanism. Thus one may think of two possible routes to collective oscillations in excitatory quorum-sensing populations: i) adaptation-led signal amplification with a fast diffusing chemical that averages out noise effects in sporadic firing; ii) increase in the ambient signal level that sends individual cells into the limit cycle state when they are less adaptive. They can be distinguished by performing single-cell experiments illustrated in Fig. S1.

bioRxiv preprint doi: https://doi.org/10.1101/421586; this version posted September 19, 2018. The copyright holder for this preprint (which was not certified by peer review) is the author/funder. All rights reserved. No reuse allowed without permission.

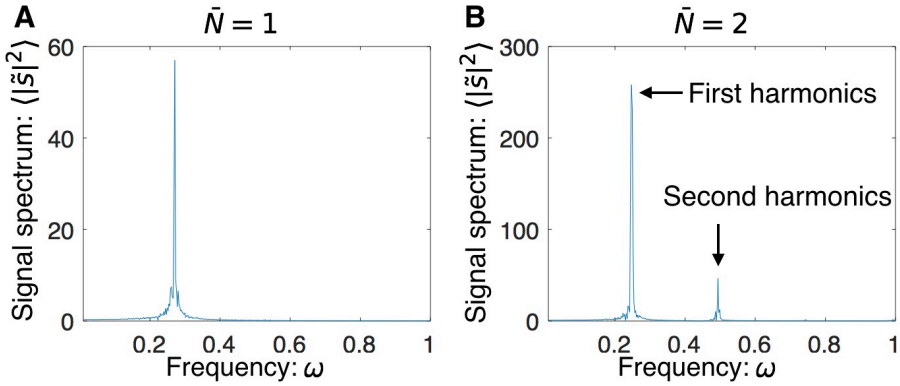

FIG. S4. **Power spectra of the signal from simulations of the coupled FHN model**. (**A**) At $\bar{N} = 1$ which is just above the onset of collective oscillations, the spectrum is dominated by the first harmonic. (**B**) At $\bar{N} = 2$, spectral weight around the second harmonic becomes significant. Other parameters are the same as in Fig. S2.

B. Collective oscillations in a synthetic circuit

Danino *et al.* reported the first experiment where a synthetic gene circuit was used to achieve collective oscillations in bacterial cell populations [17]. Their design employed plasmids that carry genes for the synthesis (luxI) and degradation (aiiA) of the quorum sensing molecule acyl-homoserine lactone (AHL). Feedback is achieved by regulating the promoter activity of these genes in an AHL-dependent manner. The interaction scheme is illustrated in Fig. S5**A**, where the concentrations of the enzymes as well as the intracellular and extracellular AHL molecules are indicated. As the AHL molecule freely diffuses across the cell membrane, different cells are coupled via the extracellular AHL whose concentration is controlled externally in a microfluidic setup by adjusting the flow rate.

Danino *et al.* proposed the following model to interpret their experimental results [17]:

$$\frac{dA}{dt} = C_A[1-(d/d_0)^4]P(\alpha,\tau) - \frac{\gamma_A A}{1+f_0\times[A+I]}, \tag{S2a}$$

$$\frac{dI}{dt} = C_I[1-(d/d_0)^4]P(\alpha,\tau) - \frac{\gamma_I I}{1+f_0\times[A+I]}, \tag{S2b}$$

$$\frac{dH_i}{dt} = \frac{bI}{1+kI} - \frac{\gamma_H A H_i}{1+gA} + D[H_e - H_i], \tag{S2c}$$

$$\frac{\partial H_e}{\partial t} = -\frac{d}{1-d}D[H_e - H_i] - \mu H_e + D_1\frac{\partial^2 H_e}{\partial x^2}. \tag{S2d}$$

where $P(\alpha,\tau)$ describes a delayed promoter response to the intracellular AHL concentration H_i. Denoting $H_i(t-\tau)$ by H_τ, we have

$$P(\alpha,\tau) = \frac{\delta + \alpha H_\tau^2}{1+k_1 H_\tau^2}.$$

d is the rescaled cell density (ranging from 0 to 1); D is the permeability coefficient of AHL across the cell membrane; D_1 is the diffusion coefficient in the intercellular medium; μ is the AHL degradation rate (controlled by the flow rate around the chamber where cells accumulate).

Fig. S5**B** shows the response of H_i to a sudden ramp in H_e, during which the AHL flow across the cell membrane reverses its direction. A further increase in H_e will not significantly push up H_i. On the other hand, due to the delayed promoter activity and the fast LuxI response ($C_I > C_A$), a transient and strong response of H_i is possible, as the data in Fig. S5**B** shows. Therefore, H_i can be considered as an intracellular observable that responds adaptively to the intercellular signal H_e.

Fig. S5**C** shows the trajectories of H_e and H_i at different values of the cell density d, obtained from numerical integration of Eqs. (S2). Collective oscillations are observed at intermediate cell densities or coupling strength $\bar{N} = D^2 d/(1-d)$. The oscillation frequency first decreases with the cell density, but increases again before quenching takes place (Fig. S5**D**). One interesting phenomenon observed experimentally is that the oscillation frequency decreases with increasing flow rate μ, while the decay rate $\omega_s = \mu + Dd/(1-d)$ of H_e increases. This seems to contradict with the phase matching scheme we introduced to determine ω_o. However, we note that an increase in μ decreases

bioRxiv preprint doi: https://doi.org/10.1101/421586; this version posted September 19, 2018. The copyright holder for this preprint (which was not certified by peer review) is the author/funder. All rights reserved. No reuse allowed without permission.

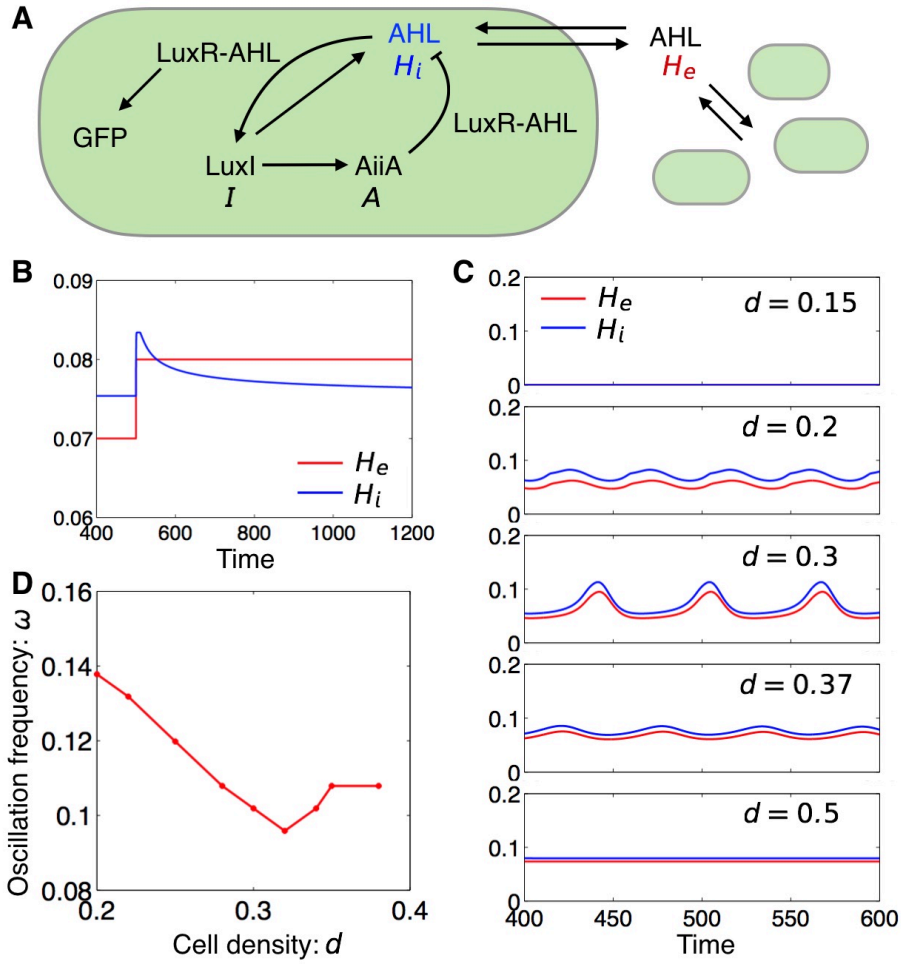

FIG. S5. **Collective oscillations of coupled synthetic quorum sensing circuits.** (**A**) The design and coupling of the synthetic circuits. Here, H_e is the concentration of the extracellular AHL, which is our signal; and H_i is the intracellular AHL concentration, which is our adaptive observable. (**B**) The response of the internal AHL concentration when we enforce a step change of the extracellular AHL concentration. Partial adaptation is observed at various cell density d's. (**C**) The system dynamics at various cell density d. (**D**) The oscillation frequency at various cell densities. The frequency first decreases, and then increases. Other parameters: $C_A = 1$, $C_I = 4$, $\delta = 10^{-3}$, $\alpha = 2500$, $\tau = 10$, $k = 1$, $k_1 = 0.1$, $b = 0.06$, $\gamma_A = 15$, $\gamma_I = 24$, $\gamma_H = 0.01$, $f_0 = 0.3$, $g = 0.01$, $d_0 = 0.88$, $D = 2.5$, $D_1 = 0$, $\mu = 0.2$. Parameters are the same as used in [17].

H_e which in turn decreases the average H_i. This can slow down the intracellular response considerably, leading to a longer oscillation period.

C. Glycolytic oscillations in yeast cells

Glycolytic oscillations in dense yeast cell suspensions have been known for a long time [18]. The phenomenon at cellular level is complex not only because of a large number of enzymes and metabolites involved, but also a multitude of regulatory interactions whose activation pattern and strength are not well understood. Furthermore, flux diversion into side branches other than the main fermentative pathway can significantly attenuate or even diminish the oscillations. Yet the oscillations are easy to produce following the standard experimental protocols, suggesting that certain type of low dimensional mechanism inside a cell such as energy or redox balance is at work.

In the following we explore the possibility of an adaptation route to yeast glycolytic oscillations. It is known that yeast cells communicate through the intercellular acetaldehyde (ACE) which acts as a redox signal. The intracellular redox ratio NAD/NADH affects the rate of the key reaction GAPDH separating ATP consuming and ATP harvesting parts of the glycolytic pathway. Adaptation of the glycolytic flux to a rising (or receding) ACE level may result from the combined action of regulatory interactions to maintain ATP homeostasis. We verify the above scenario in

bioRxiv preprint doi: https://doi.org/10.1101/421586; this version posted September 19, 2018. The copyright holder for this preprint (which was not certified by peer review) is the author/funder. All rights reserved. No reuse allowed without permission.

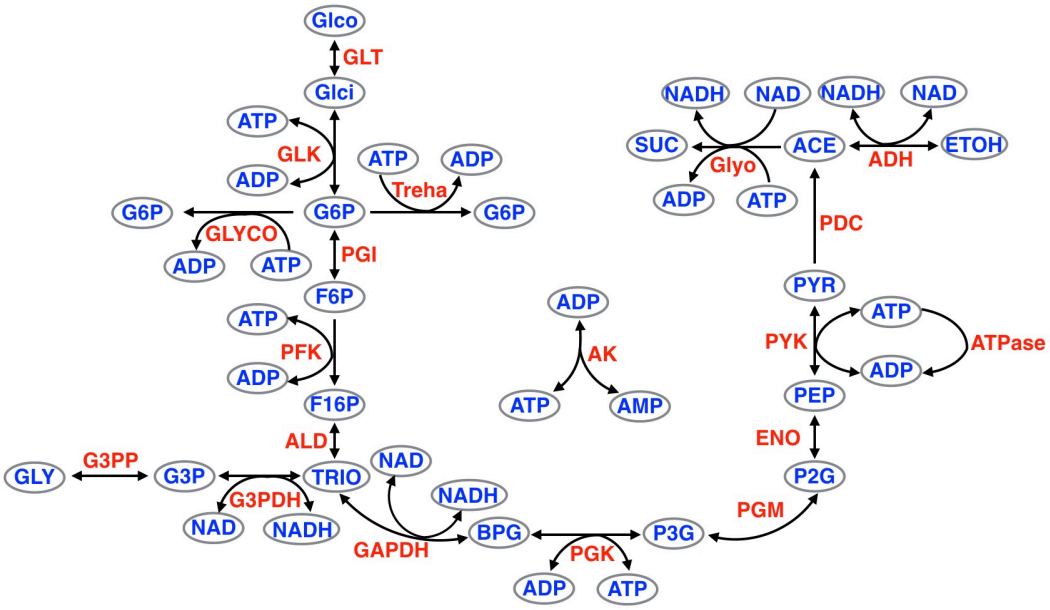

FIG. S6. **The network of reactions in a detailed model of glycolysis [19]**. Letters in blue denote metabolites, while those in red are the reactions. Directional (bidirectional) arrows indicate irreversible (reversible) reactions. Abbreviations: Glco, glucose; ACE, acetaldehyde, ADH, alcohol dehydrogenase; AK, adenylate kinase; ALD, fructose-1,6-bisphosphate aldolase; BPG, 1,3-bis-phosphoglycerate; ENO, phosphopyruvate hydratase; F16P, fructose-1,6-bisphosphate; F6P, fructose 6-phosphate; GAPDH, D-glyceraldehyde-3-phosphate dehydrogenase (phosphorylating); G3P, glycerol 3-phosphate; G3PDH, glycerol 3-phos- phate dehydrogenase; G6P, glucose 6-phosphate; GLYCO, glycogen branch; GLK, glucokinase (a hexokinase); P2G, 2-phosphoglycerate; P3G, 3-phosphoglycerate; PEP, phosphoenolpyruvate; PDC, pyruvate decarboxylase; PGI, glucose-6-phosphate isomerase; PFK, 6-phosphofructokinase; PGK, phosphoglycerate kinase; PGM, phosphoglycerate mutase; PYK, pyruvate kinase; PYR, pyruvate; Treha, trehalose branch; SUC, succinate branch; Glyo, glyoxylate shunt.

a detailed model proposed by du Preez et al. [19] (referred to as the full model), and then develop a minimal model that captures the main features of the response phase diagram of the full model. Owing to its conceptual simplicity, the minimal model can be employed for semi-quantitative interpretation of experimental findings and for the design of future experiments.

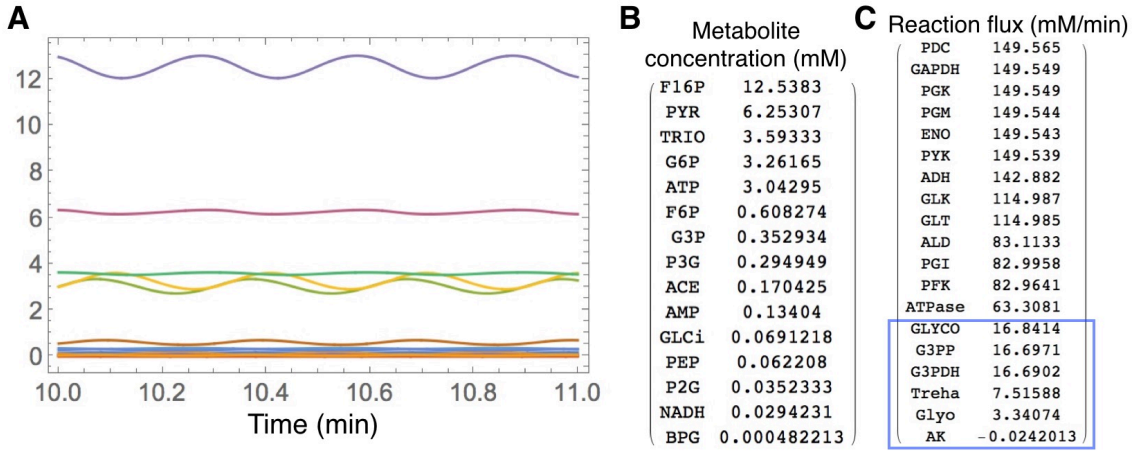

FIG. S7. **Spontaneous oscillations in the full model**. (**A**) Trajectories of all metabolites at glucose concentration Glco=10. (**B**) and (**C**) Time-averaged metabolite concentrations and reaction fluxes in descending order.

bioRxiv preprint doi: https://doi.org/10.1101/421586; this version posted September 19, 2018. The copyright holder for this preprint (which was not certified by peer review) is the author/funder. All rights reserved. No reuse allowed without permission.

1. *Single-cell perturbation study*

The full intracellular reaction network of the kinetic model by du Preez et al. [19] is shown in Fig. S6. It contains around 20 reactions and 15 metabolite concentrations as dynamical variables. The reaction fluxes are highly nonlinear functions of these variables. Predictions of the model were shown to agree semi-quantitatively with experimental data on yeast glycolytic oscillations [20]. Below we use the same parameter values as adopted in the original model termed dupree2 in [19], unless otherwise stated.

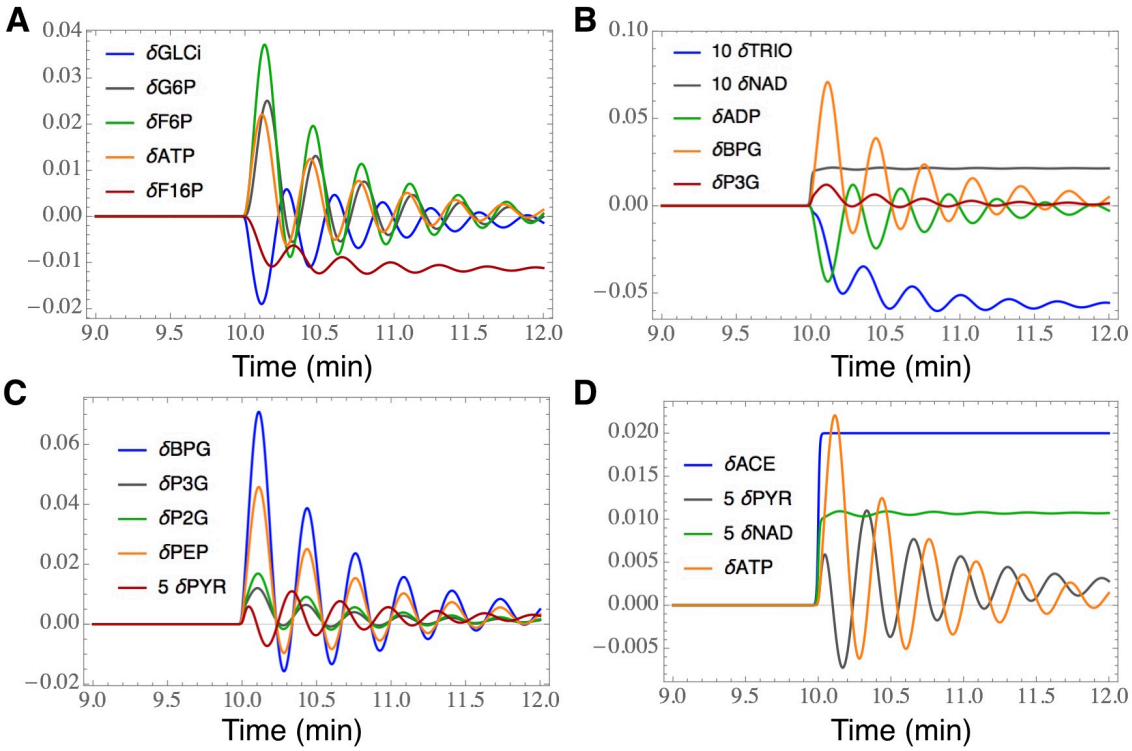

FIG. S8. **Response of metabolites to a redox signal at low ACE concentrations**. Here, $\mathrm{ACE}(t) = \mathrm{ACE}_0[1+0.02H(t)]$, with $H(t)$ being a Hill function with a large Hill coefficient. The notation δx of a variable x represents its relative change from a pre-stimulus level $\bar{x}$, i.e., $\delta x \equiv [x(t) - \bar{x}]/\bar{x}$. Quantities such as PYR and NAD which have too small values are amplified to make them visible on the plot. (**A**) The response of metabolites around G6P in the upper section of the glycolytic pathway; (**B**) The response of metabolites around BPG in the middle section of the glycolytic pathway; (**C**) The response of metabolites from BPG to PYR in the lower section of the glycolytic pathway; and (**D**) The response of metabolites in the downstream fermentation pathway. Parameters: $\mathrm{ACE}_0 = 0.05$ and $\mathrm{Glco} = 10$.

Fig. S7 shows an oscillatory solution of the model at the glucose concentration Glco =10 mM. The oscillation frequency is $\omega_0 \approx 21$ min^{-1}, corresponding to a period of $\tau_0 \simeq 0.3$ min. The mean concentration of ACE is 0.17 mM (Fig. S7**B**). Reaction fluxes are concentrated along the linear pathway from Glco to ETOH, while the side reactions carry very little flux (Fig. S7**C**, blue box). Below, we present response properties of the model using ACE concentration as the second control variable, in addition to the extracellular glucose concentration. Time is measured in minutes and concentrations in mM.

To move out of the oscillatory regime, we lower the mean acetaldehyde concentration to $\mathrm{ACE}_0 = 0.05$. Experimentally, this can be achieved by adding cyanide (KCN) which reacts with ACE in the solution [21]. Fig. S8 shows the time course of metabolites under a step-wise increase in the ACE concentration. The four panels are organized following the order of metabolites along the glycolytic pathway, with the addition of ATP, ADP and NAD. Most metabolites adapt at least partially, except F16P and TRIO upstream of the reaction GAPDH that uses NAD and NADH as cofactors. The redox pair NAD and NADH, being tightly connected to ACE, do not adapt either.

We now consider oscillations of the same set of metabolites stimulated by a periodic redox signal at the frequency ω_0 of spontaneous oscillations mentioned above. In Fig. S9**A**, ATP, G6P and F6P are approximately in phase with each other, but they are out of phase with Glci at the entry point of the pathway. The non-adaptive F16P has a behavior of its own. The phase relations for these metabolites have been measured experimentally, and the results agree well with our numerics [22]. In Figs. S9**B**-**C**, metabolites from BPG down to PEP share nearly the same phase

bioRxiv preprint doi: https://doi.org/10.1101/421586; this version posted September 19, 2018. The copyright holder for this preprint (which was not certified by peer review) is the author/funder. All rights reserved. No reuse allowed without permission.

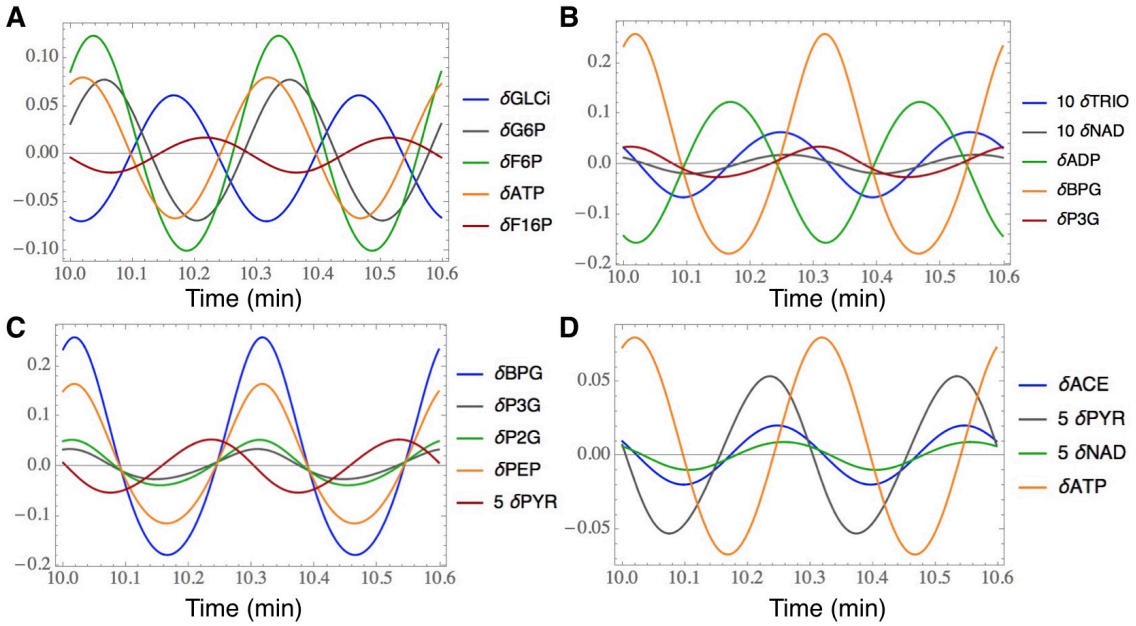

FIG. S9. **Concentration variations along the glycolytic pathway stimulated by a periodic redox signal**. Here, $\mathrm{ACE}(t) = \mathrm{ACE}_0[1 + 0.02\sin(\omega t)]$. Organization of metabolites in panels (**A**)-(**D**) is the same as in Fig. S8. Parameters: $\mathrm{ACE}_0 = 0.05$, Glco $= 10$, and $\omega = 21$.

with each other and with ATP. The non-adaptive TRIO lags slightly behind F16P. In Fig. S9**D**, PYR at the end of the glycolytic pathway has an approximately 90° phase lead over ATP, and furthermore a smaller phase lead over ACE and NAD.

Fig. S10 shows the phase shifts of metabolites against a sinusoidal signal ACE obtained from our numerical simulations over a broad frequency range. Apart from PYR, the phase relationships among metabolites at ω_0 hold also at lower frequencies. In Fig. S10**B**, it is seen that NAD has essentially the same phase as ACE in the frequency interval, while NADH is completely out of phase. Therefore, on the timescale τ_0, the phase information of ACE is passed without delay onto the redox ratio NAD/NADH, and fed into the network through the reaction GAPDH. Around ω_0, the phase lead of NADH over ACE is slightly below 180°, as observed in experiments on glycolytic oscillations [23]. Fig. S10**C** shows the downstream metabolites from BPG to PEP oscillate in phase with each other for $\omega \leq \omega_0$, meaning the internal time scales for this part of the pathway are shorter than τ_0. In contrast, PYR develops a phase lead in the intermediate frequency regime, as indicated by the two black arrows in Fig. S10**C**. (Note that in Fig. 4**D** of the Main Text, the phase lead extends to zero frequency indicating that the width of the regime depends on the glycolytic flux.) The adaptive variable ATP also has a phase lead in the entire low frequency region.

Fig. S10**D** shows the following phase relations between ATP and several other metabolites as summarized by the equations below,

$$\phi_{ATP} = \pi + \phi_{ADP} = \pi + \phi_{AMP} \approx \phi_{BPG} \approx \phi_{PEP} \approx \pi + \phi_{GLCi}. \tag{S3}$$

The first two relations among the nucleotides ATP, ADP and AMP simply reflect the conservation of their total number, and that the fraction of AMP is much lower than the other two. In-phase relations apply to substrates BPG and PEP of the ATP harvesting reactions PGK and PYK, respectively, while the out-of-phase relation is observed for GLCi in the ATP consuming reaction GLK. The fact that these relations hold almost strictly in the entire frequency region suggests that quasi-steady-state conditions apply to these and neighboring reactions. It also suggests a prominent role of ATP in synchronizing the phase of metabolites distributed along the glycolytic pathway.

In summary, our numerical results suggest the following mechanism of adaptation. Under a stepwise increase of ACE concentration, the information is passed with negligible delay to the redox ratio NAD/NADH, and then through the delayed reaction GAPDH to BPG and PEP, and transiently boosting ATP production. The transient increase of ATP concentration then reduces the upstream glycolytic flux by inhibiting the reaction PFK, which in turn decreases the downstream TRIO concentration, eventually returning the GAPDH flux to its pre-stimulus level. Although many metabolites adapt, the negative feedback loop of ATP production appears to be the core. Fig. 4**B** in the Main Text shows a more complete phase diagram of the response properties at other values of ACE_0 and Glco concentrations, including the regime of spontaneous oscillations.

bioRxiv preprint doi: https://doi.org/10.1101/421586; this version posted September 19, 2018. The copyright holder for this preprint (which was not certified by peer review) is the author/funder. All rights reserved. No reuse allowed without permission.

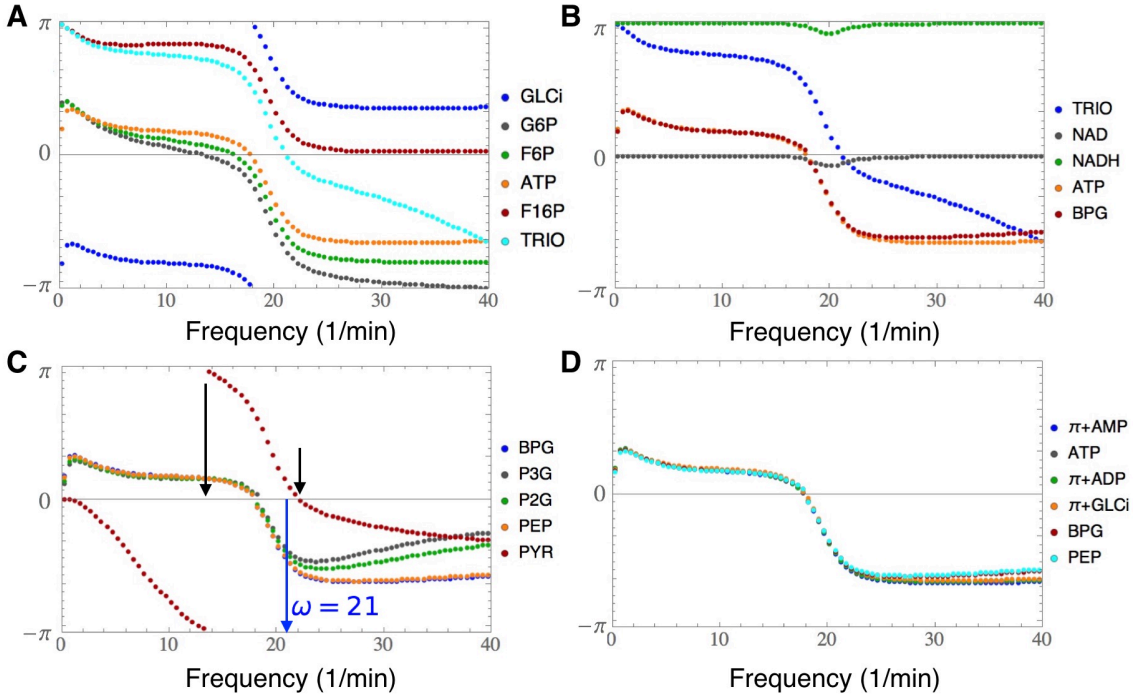

FIG. S10. **Phase shifts of metabolites against the frequency of a sinusoidal ACE signal**. (**A**) Metabolites in the "preparatory phase" of the glycolytic pathway, where ATP is consumed to activate the 6-carbon ring molecule. (**B**) Substrate, product and cofactors of the reaction GAPDH that act as the receptor of the redox signal, together with ATP. (**C**) Metabolites in the "payoff phase" of the glycolytic pathway, where ATP is harvested. For the particular values of the extracellular glucose and acetaldehyde chosen, phase lead of PYR over ACE occurs in the range of frequencies delimited by black arrows. The blue arrow indicates the intrinsic frequency studied in Fig. S9. (**D**) Metabolites that appear in Eq. (S3). The phase shift of a number of metabolites shows a dip at the low frequency end, indicating a small but finite adaptation error. Parameters: $\mathrm{ACE}_0 = 0.05$, $\mathrm{Glco} = 10$.

2. *A minimal model for glycolytic oscillations*

We constructed a minimal model to test various quantitative aspects of the adaptation mechanism described above. Reduction in the number of dynamic variables is achieved by lumping consecutive metabolites along the linear pathway that are phase synchronized into a single variable denoting their total concentration. This is a reasonable approximation when interconversion among these metabolites is much faster than the time of interest, e.g. the oscillation period. Fig. S11**A** illustrates the selected variables and their interactions. Here, y represents intermediate metabolites that do not adapt (F16P and TRIO), thereby playing the role of a memory node. The variable z represents metabolites from BPG to PEP along the glycolytic pathway. The ATP concentration is denoted by a, while the concentration of PYR, substrate for the ACE producing reaction PDC, is denoted by o. Since NAD (NADH) is always in phase (out of phase) with ACE, we adopt the redox ratio NAD/NADH as the signal s instead. Motivated by a phenomenological two-component model for glycolytic oscillations in [24], we introduce a minimal model of glycolysis with redox control as follows:

$$\tau \dot{y} = \frac{2a}{1+a^{2h}} - (\alpha_1 s + c_0)y - \epsilon y, \tag{S4a}$$

$$\tau \dot{z} = (\alpha_1 s + c_0)y - \frac{2z}{1+a^2}, \tag{S4b}$$

$$\tau \dot{a} = -\frac{2a}{1+a^{2h}} + 2\frac{2z}{1+a^2} - \frac{2a^2}{1+a^2}. \tag{S4c}$$

Here, $2a/(1+a^{2h})$ gives the reaction flux of PFK that consumes ATP and is also inhibited by ATP at high concentrations, with the inhibition strength set by the exponent $h(>1/2)$. The term $(\alpha_1 s + c_0)y$ gives the reaction flux of

bioRxiv preprint doi: https://doi.org/10.1101/421586; this version posted September 19, 2018. The copyright holder for this preprint (which was not certified by peer review) is the author/funder. All rights reserved. No reuse allowed without permission.

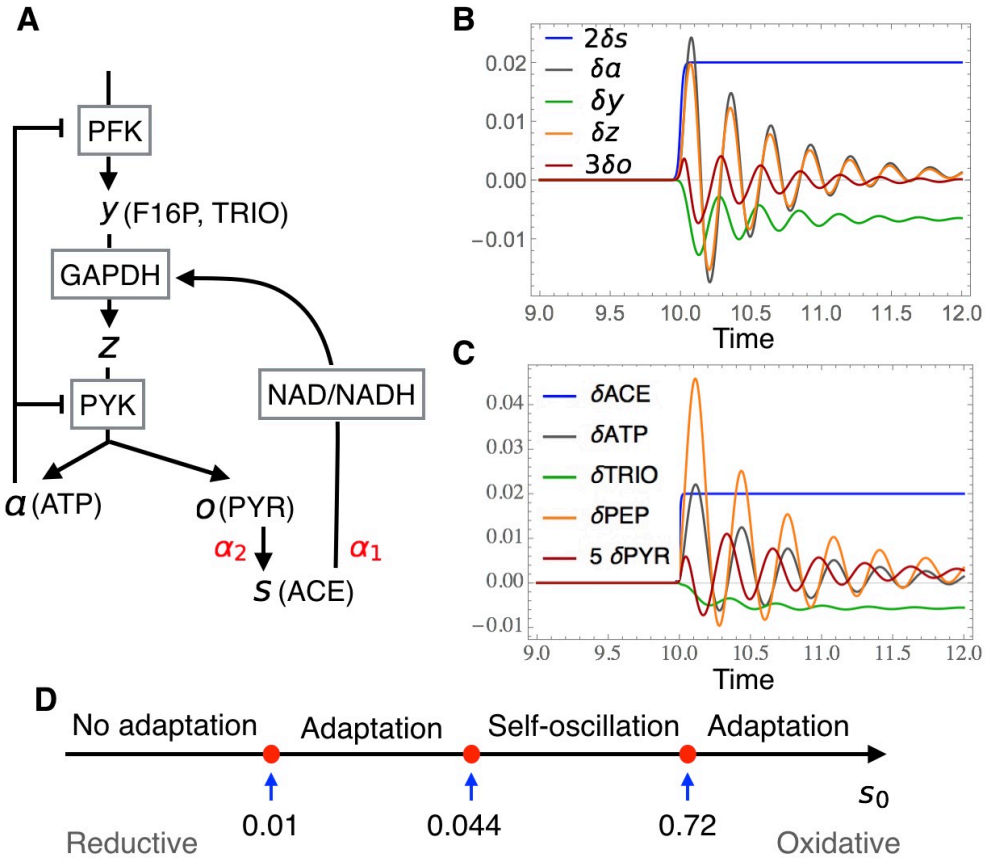

FIG. S11. **A minimal model of glycolysis with redox control**. (**A**) The network of metabolites (symbols) and reactions (boxes). (**B**) Response of metabolites upon a stepwise perturbation $s(t) = 0.04(1 + 0.01H(t))$. (**C**) Response of corresponding metabolites in the full model computed using parameter values given in FIG. S8. (**D**) Response properties of the minimal model as the intracellular redox state changes from reductive to oxidative (left to right). Parameters: $h = 3, \alpha_1 = \alpha_2 = 1$, $\tau = 0.01$, $c_0 = 0.02$, and $\epsilon = 0.01$.

GAPDH, where c_0 sets the "basal" enzyme velocity at $s = 0$. Leakage of TRIO into the side branch is given by ϵy. The term $2z/(1 + a^2)$ gives the reaction flux of PYK (and also PGK), which produces ATP but is also inhibited by ATP. In Eq. (S4c), the stoichiometric factors 1 and 2 in the first two terms on the right-hand-side correspond to the ATP consumption and production upstream and downstream of TRIO, respectively. ATP consumption by the cell outside of glycolysis is modeled by the term $2a^2/(1+a^2)$, which grows with the ATP concentration until saturation at a maximal value 2. The output variable o (PYR) is produced by the same flux that produces a (ATP) and degraded at a constant rate α_2,

$$\tau \dot{o} = \frac{2z}{1 + a^2} - \alpha_2 o. \tag{S4d}$$

For simplicity, we have chosen the time constants on the left-hand-side of the equations to be the same. As we show below, this choice is adequate for recovering the main low frequency properties of the full model.

Fig. S11**B** shows the response of the dynamical variables to a sinusoidal redox variation centered around $s_0 = 0.04$. Except the buffer variable y, all other variables show adaptive behavior, with o gaining a phase lead of 90° over a. For comparison, we show in Fig. S11**C** the response properties of corresponding metabolites in the full model in the adaptive regime, which are indeed quite similar. We have examined the response properties of the minimal model at other values of s_0 and identified four qualitatively different regimes as shown in Fig. S11**D**. As in the case of the full model (Main Text, Fig. 4**B**), spontaneous oscillations (i.e., limit cycle solution) occur at intermediate values of s_0, flanked by adaptive but non-oscillatory regimes.

We note in passing that the two-component model of Chandra et al. [24] also exhibits spontaneous oscillations when the rate constant k of the pyruvate kinase reaction (PYK in Fig. S11**A**) takes on intermediate values. As k affects the delay time of the negative feedback control in ATP production, in this sense it plays a similar role as s_0.

bioRxiv preprint doi: https://doi.org/10.1101/421586; this version posted September 19, 2018. The copyright holder for this preprint (which was not certified by peer review) is the author/funder. All rights reserved. No reuse allowed without permission.

However, our model contains an additional buffer node TRIO which is necessary for the adaptive behavior seen in Fig. S11. We have also made the ATP consumption rate dependent on the ATP concentration to eliminate certain pathological features of the Chandra et al. model at low values of a. Furthermore, our numerical analysis suggests that a sufficiently small but finite adaptation error ϵ associated with low flux diversion is needed to reproduce the response diagram Fig. S11**D**. On the high (oxidative) end of s_0, the reaction GAPDH drives down y (TRIO) and hence the flux of the side reaction, making the system adaptive even at moderate values of ϵ.

Comparing the response diagrams of the minimal model (Fig. S11**D**) and of the full model (Main Text, Fig. 4**B**), we see that the adaptive regime on the oxidative side is restricted to a much narrower region in the latter case. Upon a detailed investigation of the full model we found that, at higher values of ACE_0, the side reaction Glyo is activated. As this reaction uses both NAD and ATP as cofactors, its inclusion introduces additional feedback loops to the minimal model of Fig. S11**A**. In such a situation, variation of the extracellular ACE concentration does not translate directly to a shift of the NAD/NADH ratio through the reaction ADH. After removing the side branch Glyo in the full model, we obtained a response diagram similar to that of the minimal model (Fig. S12).

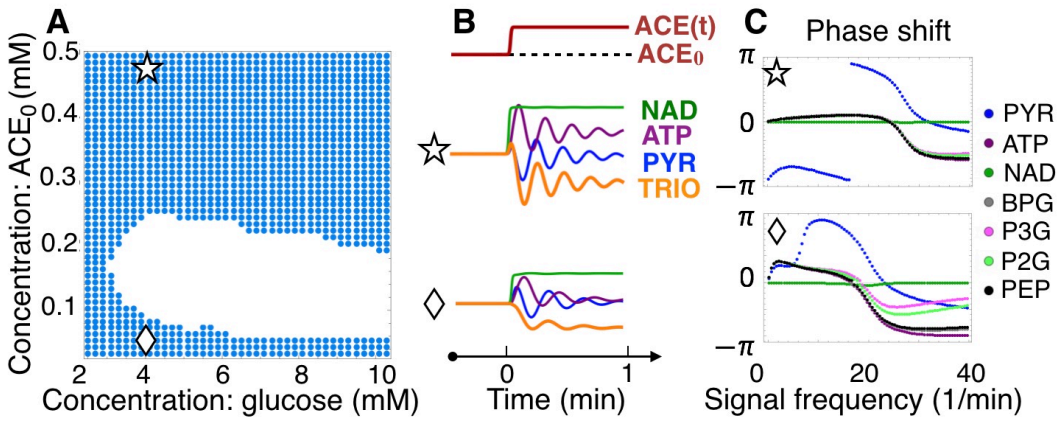

FIG. S12. **Phase diagram of the modified glycolysis model with blocked Glyo reaction**. Adaptation of PYR and ATP coexist for large ACE_0, which is consistent with our minimal model.

Fig. S13 shows representative time courses of the PYK reaction flux to a stepwise ACE signal, computed using the original and modified glycolysis model, as well as the minimal model. The original and modified models exhibit nearly identical adaptive response on the low ACE (reductive) side, but differ on the high ACE (oxidative) side. The concentration of PYR is found to be proportional to the PYK reaction flux in all three models, i.e., the degradation rate of PYR is a constant. Further numerical investigations of the full model with blocked glyoxylate shunt (Glyo) show that it shares the following features of the minimal model as the oxidation level increases: 1) the frequency inside the oscillatory regime increases; 2) (mean) a (ATP) and z (BPG, P3G, P2G, and PEP concentrations) increase by a moderate amount; 3) y (TRIO and F16P concentrations) decreases; 4) o (PYR concentration) first increases, then decreases. Experimental time-course measurement with blocked glyoxylate shunt will serve to validate or improve the model assumptions.

To study collective oscillations in a population of cells whose internal dynamics follows Eqs. (S4), we adopt the following signal dynamics as in Ref. [25]:

$$\tau_s \dot{s}_{in} = \alpha_2 o - k_{in} s_{in} - D(s_{in} - s_{ex}), \tag{S5a}$$

$$\tau_s \dot{s}_{ex} = \phi D(s_{in} - s_{ex}) - k_{ex} s_{ex}. \tag{S5b}$$

Here s_{in} and s_{ex} are the intracellular and extracellular signal concentration, respectively; D is the membrane permeability of the signaling molecule; k_{in} and k_{ex} are the intracellular and extracellular signal degradation rate; and ϕ is the volume fraction of yeast cells, which increases with the cell density, and saturates at 1. The extracellular signal strength (i.e., acetaldehyde concentration) in the coupled system is a function of ϕ.

Let us first consider the situation of fast equilibrium between s_{in} and s_{out}. Previously, Silvia De Monte *et al.* proposed a diffusion timescale $\tau \approx 0.003$ s by assuming a quasi-stationary concentration profile and that ACE molecules need to diffuse across a spherical shell with an inner radius $r_1 = 3$ μm and an outer radius $r_2 = 6.5$ μm [26]. This diffusion timescale is much smaller than the oscillation period of 37 s. Assuming the time for an ACE molecule to cross the cell membrane is of the order of 1 s or less, we obtain the following approximate equation for $s = (s_{in} + s_{ex})/2$,

$$\tau_s \dot{s} = \frac{\phi}{1+\phi} \alpha_2 o - \Big(\frac{\phi k_{in} + k_{ex}}{\phi + 1} \Big) s. \tag{S6}$$

bioRxiv preprint doi: https://doi.org/10.1101/421586; this version posted September 19, 2018. The copyright holder for this preprint (which was not certified by peer review) is the author/funder. All rights reserved. No reuse allowed without permission.

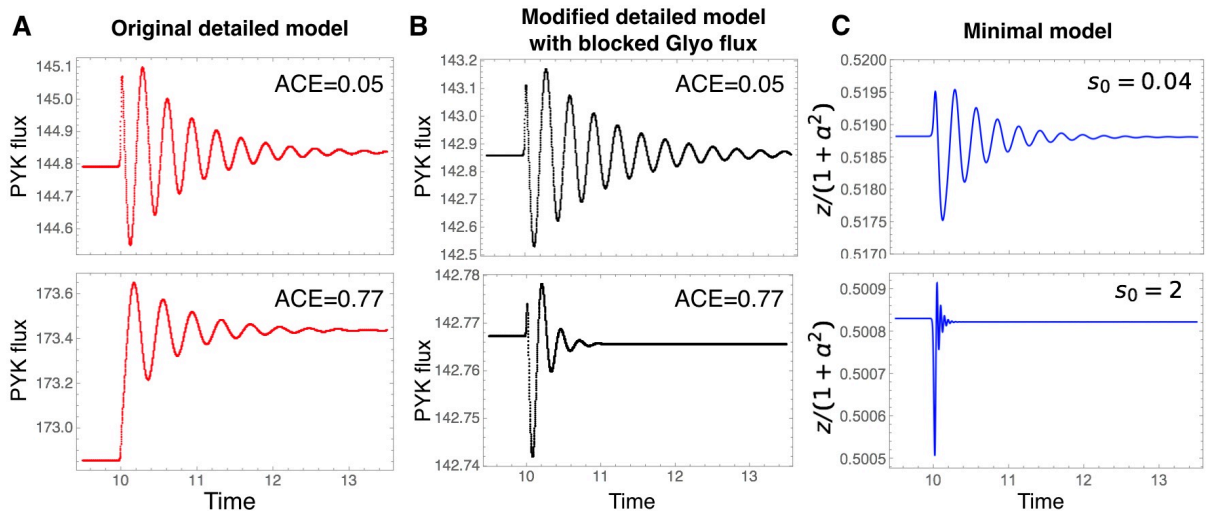

FIG. S13. **The response of PYK flux to a step perturbation of ACE at** $t = 10$. (**A**) The response of the original full model at ACE=0.05 and 0.77, respectively. (**B**) The response of the modified full model with blocked Glyo reaction at ACE=0.05 and 0.77, respectively. (**C**) The response of the minimal model. Parameters: Glco=10 for (**A**) and (**B**); the parameters for the minimal model are the same as in Fig. S11.

Up to corrections of order ϵ, the stationary state of the dynamical system defined by Eqs. (S6) and (S4) is given approximately by,

$$a \approx 1, \quad z \approx 1, \quad y \approx \frac{1}{\alpha_1 s + c_0}, \quad o \approx \frac{1}{\alpha_2}, \quad s \approx \frac{\phi}{\phi k_{in} + k_{ex}}. \tag{S7}$$

The signal strength increases with the volume fraction and saturates at $1/(k_{in}+k_{ex})$. At small but finite ϵ, corrections to the above expressions become significant at large y or small s, i.e., diversion of the glycolytic flux through the reaction G3PDH in Fig. S6. In the numerical studies presented below, we set the two ACE degradation rates k_{in} and k_{ex} to be small so that the signal strength s varies over a broad range as the cell volume fraction ϕ increases.

Fig. S14 shows numerical solutions of the coupled minimal model at four selected ϕ values. Except the case at $\phi = 0.01$, oscillations of s and the intracellular variables are seen. In Fig. S15, we plot the oscillation amplitudes and time-averaged values of s and O against the cell volume fraction ϕ. From the lower panel of Fig. S15**A** we see that, for the signal dynamics chosen, the lower adaptive regime in Fig. S11**D** is mapped to a narrow interval of cell volume fraction $0.003 < \phi < 0.013$. From Fig. S14, we see that onset of collective oscillations in the coupled system takes place between $\phi = 0.01$ and 0.013. More detailed studies indicate that the transition is not the expected Hopf bifurcation type, but instead emergence of a limit cycle at finite amplitude. Similar behavior was seen in the study of the full kinetic model (see Fig. 10 in [20]). On the other hand, experimental work seem to support the Hopf bifurcation scenario [26, 27]. We leave this issue to future investigations.

Beyond the onset point, oscillation amplitudes vary continuously with the cell density. For $\phi > 0.34$, the time-averaged value of s falls in the upper adaptive regime in Fig. S11**D**. Since the cell density here already exceeds the threshold value required for collective behavior of adaptive units, oscillations continue.

Finally, we present some numerical results demonstrating the effect of a slower cross-membrane transport of acetaldehyde on the collective dynamics. The system dynamics is defined by Eqs. (S4)] for individual cells (with $s = s_{in}$) together with Eqs. (S5) for the intracellular and extracellular signal concentrations. Fig. S16 shows the oscillation amplitude of s_{in} together with the time-averaged values of s_{in} and s_{out} at selected values of D. At $D = 100$ and 10, s_{in} and s_{out} are nearly identical and the system behavior is essentially the same as described above under the fast equilibrium assumption. At $D = 1$, the time-averaged value of s_{ext} is noticeably smaller than that of s_{in}, indicating a significant gradient of acetaldehyde concentration across the cell membrane. Nevertheless, collective oscillations are not much affected. Collective oscillations disappear at $D = 0.1$. Here, s_{in} remains high due to the slow intracellular degradation rate k_{in}, which places the single-cell dynamics in the upper adaptive regime even when the cell density vanishes. However, the phase delay across the cell membrane changes the response properties of the cell to external signal variations. In this case, s_{in} should be considered as the sender of the external signal but as one can see from Eq. (S5a), the adaptation of O to s_{in} does not translate to adaptation of s_{in} to s_{ex}. The latter is required for the adaptation route to collective oscillations.

bioRxiv preprint doi: https://doi.org/10.1101/421586; this version posted September 19, 2018. The copyright holder for this preprint (which was not certified by peer review) is the author/funder. All rights reserved. No reuse allowed without permission.

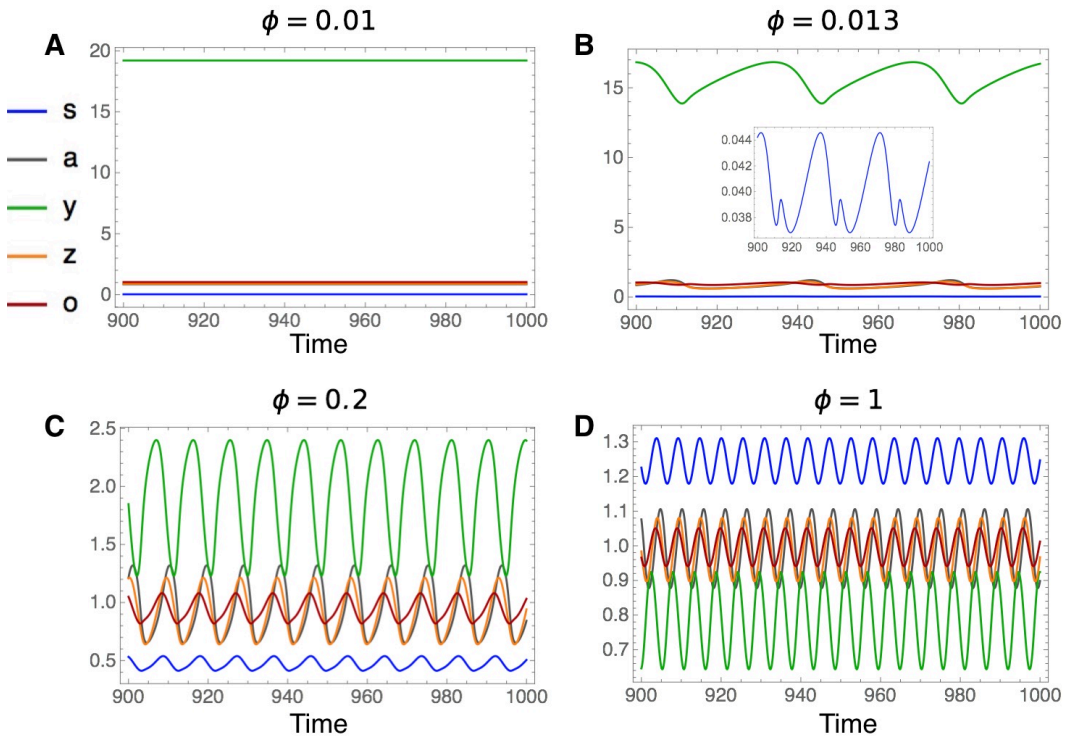

FIG. S14. **Collective dynamics of the minimal model coupled via Eq. (S6)**. (**A**)-(**D**) Temporal trajectories at selected values of the volume fraction ϕ. The same color scheme of variables is used. Inset in **B** shows the signal trajectory on an enlarged scale. Parameters: $h = 3, \alpha_1 = \alpha_2 = 1, \epsilon = 0.01$, $k_{in} = 0.5$, $k_{ex} = 0.3$, $\tau = 1$, $c_0 = 0.02$, and $\tau_s = 0.1$.

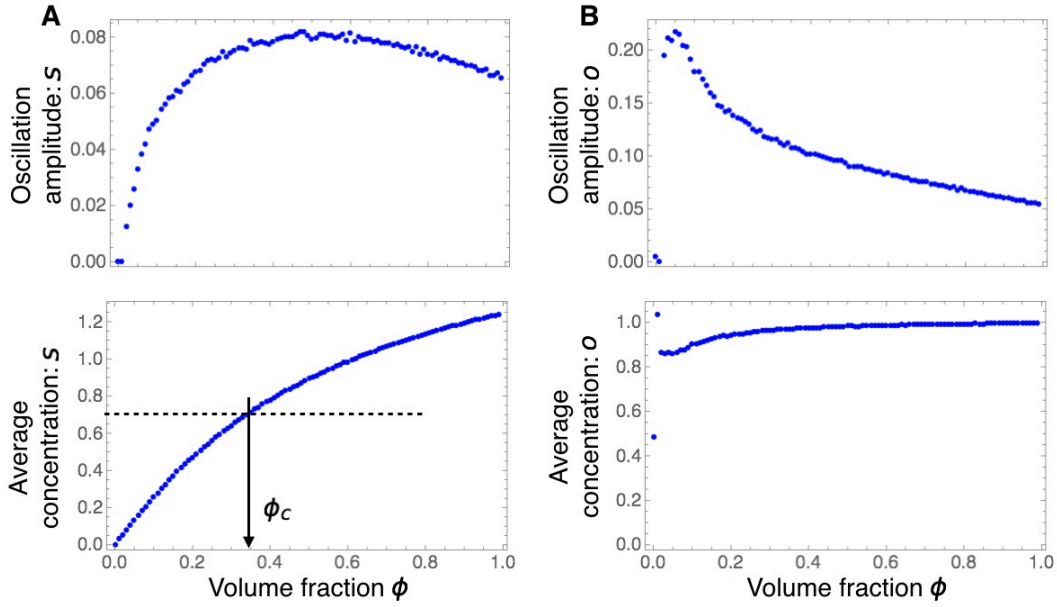

FIG. S15. **Collective oscillations against the yeast cell density**. (**A**) Upper panel: oscillation amplitude of the signal s as a function of the cell volume fraction ϕ. Lower panel: time-averaged signal concentration against ϕ. The black dashed line indicates the upper threshold value $s_c = 0.72$ where individual cells exits from the oscillatory regime under a constant external environment. (**B**) Upper panel: oscillation amplitude of the sender node o against ϕ. Lower panel: time-averaged value of o against ϕ. Parameters are the same as in Fig. S14.

In summary, under fast equilibration between intracellular and extracellular acetaldehyde concentrations, the coupled system exhibits collective oscillations over a broad range of cell densities, encompassing the adaptive and oscilla-

bioRxiv preprint doi: https://doi.org/10.1101/421586; this version posted September 19, 2018. The copyright holder for this preprint (which was not certified by peer review) is the author/funder. All rights reserved. No reuse allowed without permission.

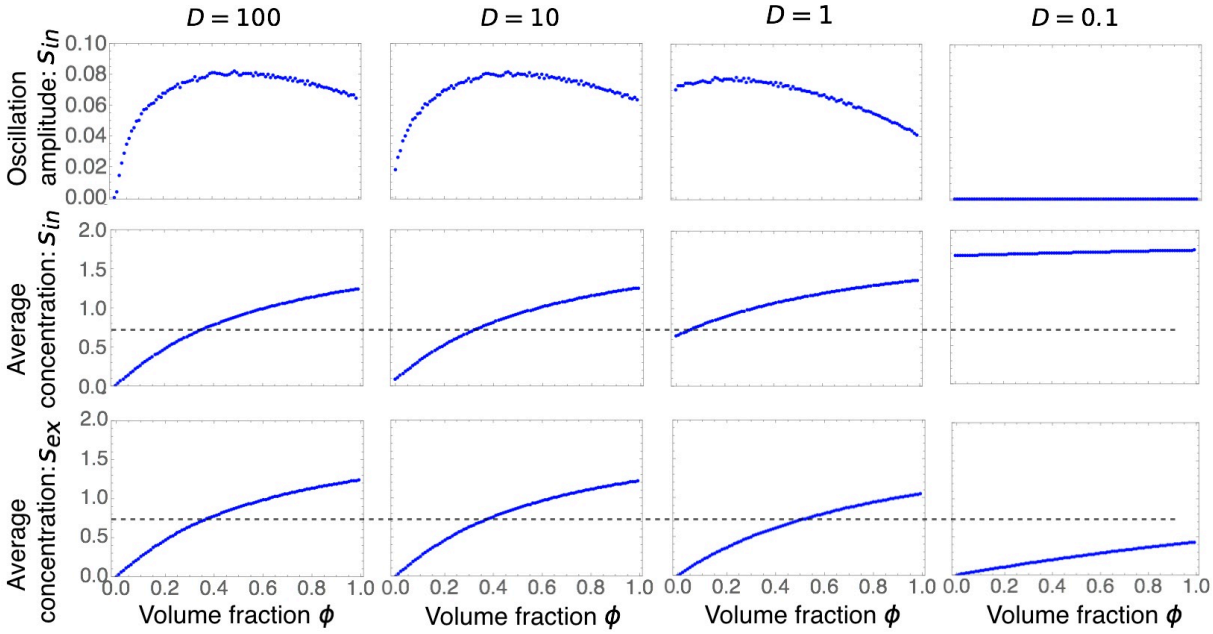

FIG. S16. **Effect of delay in cross-membrane transport of the signaling molecule on collective dynamics**. Results of numerical integration of Eqs. (S4)] coupled to the two-component signal dynamics Eq. (S5)] at selected values of $D = 100, 10, 1, 0.1$. The black dashed line indicates the signal level $s = 0.72$ marking the upper boundary between oscillatory and adaptive regimes of a single cell. Other parameters are the same as in Fig. S14.

tory regimes of a single cell. Onset of collective oscillations at low cell densities exhibit complex behavior due to the assumed sensitivity of the reaction GAPDH to the NAD/NADH ratio. Delay in the cross-membrane transport of acetaldehyde weakens adaptation of intracellular metabolite concentrations to change in the extracellular acetaldehyde concentration, and may eliminate collective oscillations altogether when the delay is too long. At moderate delays, rise in the intracellular acetaldehyde concentration brings individual cells to the oscillatory even when in isolation. The enhanced oscillation amplitude at $D = 1$ and low cell densities seen in Fig. S16, however, is obtained under the assumption that all cells in the population behave identically. This behavior is susceptible to cell-to-cell variations as well as temporal noise in intracellular dynamics. Our model study exposes this and other subtleties that can affect emergence of collective oscillations. The specific effects we identified in this work could serve to guide the design of future experiments where various model parameters can be controlled quantitatively, e.g., k_{ex} for extracellular degradation rate of acetaldehyde by adjusting the flow rate in microfluidic setups [21].

[1] K. Sekimoto, *Stochastic energetics*, vol. 799 (Berlin Springer Verlag, 2010).
[2] J. Sethna, *Statistical mechanics: entropy, order parameters, and complexity*, vol. 14 (Oxford University Press, 2006).
[3] G. Lan, P. Sartori, S. Neumann, V. Sourjik, Y. Tu, *Nat. Phys.* **8**, 422 (2012).
[4] P. Sartori, Y. Tu, *Phys. Rev. Lett.* **115**, 118102 (2015).
[5] S.-W. Wang, Y. Lan, L.-H. Tang, *J. Stat. Mech.* **2015**, P07025 (2015).
[6] R. Kubo, *Rep. Prog. Phys.* **29**, 255 (1966).
[7] G. Diezemann, *Phys. Rev. E* **72**, 011104 (2005).
[8] S.-W. Wang, K. Kawaguchi, S.-i. Sasa, L.-H. Tang, *Phys. Rev. Lett.* **117**, 070601 (2016).
[9] W. Ma, A. Trusina, H. El-Samad, W. A. Lim, C. Tang, *Cell* **138**, 760 (2009).
[10] G. De Palo, R. G. Endres, *PLoS Comput. Biol.* **9**, e1003300 (2013).
[11] G. Diezemann, *Phys. Rev. E* **85**, 051502 (2012).
[12] E. M. Izhikevich, *Dynamical systems in neuroscience* (MIT press, 2007).
[13] A. E. Sgro, *et al.*, *Mol. Syst. Biol.* **11**, 779 (2015).
[14] A. Hubaud, I. Regev, L. Mahadevan, O. Pourquie, *Cell* **171**, 668 (2017).
[15] A. E. Sgro, *et al.*, *Mol. Syst. Biol.* **11**, 779 (2015).
[16] K. Kamino, *et al.*, *Proc. Natl. Acad. Sci. U.S.A.* p. 201702181 (2017).
[17] T. Danino, O. Mondragón-Palomino, L. Tsimring, J. Hasty, *Nature* **463**, 326 (2010).
[18] P. Richard, *FEMS Microbiol. Rev.* **27**, 547 (2003).

bioRxiv preprint doi: https://doi.org/10.1101/421586; this version posted September 19, 2018. The copyright holder for this preprint (which was not certified by peer review) is the author/funder. All rights reserved. No reuse allowed without permission.

[19] F. B. du Preez, D. D. van Niekerk, B. Kooi, J. M. Rohwer, J. L. Snoep, *FEBS J.* **279**, 2810 (2012).
[20] F. B. du Preez, D. D. van Niekerk, J. L. Snoep, *FEBS J.* **279**, 2823 (2012).
[21] A.-K. Gustavsson, C. B. Adiels, B. Mehlig, M. Goksör, *Sci. Rep.* **5** (2015).
[22] P. Richard, B. Teusink, M. B. Hemker, K. Van Dam, H. V. Westerhoff, *Yeast* **12**, 731 (1996).
[23] P. Richard, B. M. Bakker, B. Teusink, K. Dam, H. V. Westerhoff, *Eur. J. Biochem.* **235**, 238 (1996).
[24] F. A. Chandra, G. Buzi, J. C. Doyle, *Science* **333**, 187 (2011).
[25] J. Wolf, *et al.*, *Biophys. J.* **78**, 1145 (2000).
[26] S. De Monte, F. d'Ovidio, S. Danø, P. G. Sørensen, *Proc. Natl. Acad. Sci. U.S.A.* **104**, 18377 (2007).
[27] S. Danø, P. G. Sørensen, F. Hynne, *Nature* **402**, 320 (1999).